

SYNTHESIZING MEASUREMENT, MODELING AND REMOTE SENSING TECHNIQUES
TO STUDY SPATIOTEMPORAL VARIABILITY OF SEASONAL SNOW

by

Andrew R. Hedrick

A thesis

submitted in partial fulfillment
of the requirements for the degree of
Master of Science in Geophysics
Boise State University

December 2013

© 2013

Andrew R. Hedrick

ALL RIGHTS RESERVED

BOISE STATE UNIVERSITY GRADUATE COLLEGE

DEFENSE COMMITTEE AND FINAL READING APPROVALS

of the thesis submitted by

Andrew R. Hedrick

Thesis Title: Synthesizing Measurement, Modeling and Remote Sensing Techniques
to Study Spatiotemporal Variability of Seasonal Snow

Date of Final Oral Examination: 16 October 2013

The following individuals read and discussed the thesis submitted by student Andrew R. Hedrick, and they evaluated his presentation and response to questions during the final oral examination. They found that the student passed the final oral examination.

Hans-Peter Marshall, Ph.D. Chair, Supervisory Committee

Alejandro N. Flores, Ph.D. Member, Supervisory Committee

Adam H. Winstral, Ph.D. Member, Supervisory Committee

The final reading approval of the thesis was granted by Hans-Peter Marshall, Ph.D., Chair of the Supervisory Committee. The thesis was approved for the Graduate College by John R. Pelton, Ph.D., Dean of the Graduate College.

ACKNOWLEDGMENT

I would like to begin by thanking my advisor and mentor Hans-Peter Marshall for his overwhelmingly positive guidance and support, without which this research would not have been possible. I must also specifically thank him for allowing me the wonderful opportunities to be a part of multiple collaborative research projects; in the process meeting dozens of other like-minded snow researchers around the globe. Additionally, I would like to thank my committee members Adam Winstral and Lejo Flores for supplying their much-needed modeling expertise and for keeping me on a focused research path.

Much of the data presented in this thesis was gathered by a large team of researchers coordinated by Kelly Elder of the Fort Collins Rocky Mountain Research Station, Donald Cline of the National Weather Service, and Simon Yueh of the NASA Jet Propulsion Laboratory. I would also like to thank Nancy Glenn, Rupesh Shrestha, and Lucas Spaete of the Boise Center Aerospace Laboratory for all of their instructional assistance with LiDAR processing and acquisition.

Exhaustive field campaigns and in-depth discussions with Scott Havens and Achim Heilig over the past few years taught me much that I would not have learned in a classroom, for which I am eternally grateful. I look forward to our future collaborations. I also must thank my fellow classmates Chago Rodriguez, Mark Robertson, Andy Karlson, and Hank Hetrick for their advice and for helping me setup and maintain the time-lapse camera measurement site.

I would like to give a special thanks to my family for their continual encouragement and patience. And lastly, I could not have finished any of this work without my

partner, Rialin Flores, who has always been more than happy to listen to me prattle on about science. Thank you.

This work was made financially possible by a NASA New Investigator Program Grant (NNX10AO02G), a NASA Experimental Program to Stimulate Competitive Research (EPSCoR) Grant (NNX10AN30A), and an American Avalanche Association Student Research Grant.

ABSTRACT

Mountain snowpacks vary drastically over length scales as small as 1–2 meters in complex terrain and require high resolution measurements to accurately quantify the spatial distribution of snow. This thesis explores this spatial distribution using remote sensing, modeling, and ground-based observations. Snow depth estimates from airborne LiDAR at 5 m resolution over 750 km^2 was compared to in situ observations and results from physically-based snow and wind redistribution models, and a new low cost method for continuous depth measurements at the slope scale was developed.

Repeated airborne Light Detection And Ranging (LiDAR) surveys are capable of recording snow depth distributions at 1–5 meter resolution over very large geographic areas, while additionally providing information about vegetation, slope aspect, and terrain roughness. During NASA’s second Cold Lands Processes eXperiment (CLPX-II) in the winter of 2006/07, two LiDAR surveys were flown nearly three months apart over a vast 750 km^2 swath of the Rocky Mountains near Steamboat Springs, Colorado. Both flights took place well before any significant melt occurred, and the difference of the vegetation-filtered surfaces resulted in an estimate of the change in snow height across the survey area. An intensive manual measurement campaign was conducted to coincide with each LiDAR flight to provide ground truth information for the LiDAR dataset. Using the in situ measurements and the LiDAR-derived snow depth changes, an uncertainty study was performed to investigate errors in snow depth change for this high resolution remote sensing method due to elevation gradients and vegetation types.

Secondly, this work leverages the large extent of the CLPX-II LiDAR dataset to

validate more than 900 pixels, each at 30 arc-second resolution, of modeled snow depth from the SNOW Data Assimilation System (SNODAS) operational hydrologic model developed by the National Operational Hydrologic Remote Sensing Center (NOHRSC). Upscaling the high resolution LiDAR-derived snow depths to the much lower spatial resolution of the SNODAS estimates produced a statistically robust dataset of over 900 independent pixel comparisons for the first time, due to the difficulty in obtaining independent validation data at the 1 km scale. Results support the notion that sub pixel-scale slope, aspect, vegetation density, and terrain roughness factors are important to consider for model predictions of snow distribution in mountain regions.

To investigate the wind transport factor, a wind redistribution model based on terrain characteristics is implemented for a 1 km^2 wind-affected sub region where high resolution snow depths have been supplied from three independent LiDAR flights taken during different winter seasons. The interannual consistency of snow depths at the site reveals a close correlation with the terrain parameters produced by the wind model for a known local prevailing wind direction.

LiDAR currently remains the highest resolution large extent method for measuring snow depth, even though it is extremely costly to perform frequently and is primarily used only at intensive research sites. To monitor temporal variations of snow depth over more than a point, simple time-lapse photography is a promising and efficient way to obtain information about snowpack evolution at the slope scale. A robust and low power method to measure hourly changes in snow depth was developed that involves only three primary components: (1) an inexpensive, off-the-shelf time-lapse camera, (2) a weatherproof external battery box, and (3) an array of secured,

brightly painted depth markers. The camera is calibrated at the marker locations and a pixel counting algorithm automatically distinguishes the snow surface at each marker location after the images are captured. Results agreed closely with nearby standard ultrasonic depth sensors.

CONTENTS

ACKNOWLEDGMENT	iv
ABSTRACT	vi
LIST OF TABLES	xi
LIST OF FIGURES	xii
1 INTRODUCTION	1
2 CONSTRAINING LIDAR UNCERTAINTY WITH IN SITU MANUAL MEASUREMENTS	6
2.1 Summary	6
2.2 Introduction	7
2.3 Methods	10
2.3.1 Site Description	10
2.3.2 In Situ Measurements	11
2.4 Results	15
2.5 Discussion	23
3 USING LIDAR SNOW DEPTH INFORMATION TO VALIDATE SNODAS AND FORCE A WIND REDISTRIBUTION MODEL	25
3.1 Summary	25
3.2 Validating SNODAS	26

3.2.1	Introduction	26
3.2.2	Methods	29
3.2.3	Results	30
3.2.4	Discussion	35
3.3	High-Resolution Wind Redistribution Modeling	41
3.3.1	Introduction	41
3.3.2	Study Area	43
3.3.3	The Wind Redistribution Model	45
3.3.4	Results	47
3.3.5	Discussion	57
4	MEASURING SNOW DEPTHS WITH TIME-LAPSE PHOTOGRAPHY	60
4.1	Summary	60
4.2	Introduction	60
4.3	Methods	63
4.3.1	Study Sites	63
4.3.2	Instrumentation	66
4.3.3	Algorithm	69
4.4	Results	71
4.5	Future Work	74
5	SUMMARY AND CONCLUSIONS	75
	REFERENCES	79

LIST OF TABLES

2.1	Site descriptions for CLPX-II Intensive Observation Periods	14
-----	---	----

LIST OF FIGURES

2.1	Location of CLPX-II LiDAR footprint in Northern Colorado, USA . . .	11
2.2	LiDAR-derived change in total snow depth at 5-meter resolution for the period of December 3 rd , 2006 – February 22 nd , 2007.	12
2.3	Locations of in situ intensive observation sites within CLPX2 LiDAR footprint. Also shown are the six nearest Snow Telemetry (SNOTEL) sites maintained by the Natural Resource Conservation Service (NRCS).	12
2.4	Comparison of mean LiDAR-derived vs. mean in situ-measured snow depth change (Dec. 3 rd – Feb. 22 nd) over each of the twelve Intensive Observation Period sites.	16
2.5	a) : Fancher Area, Arapahoe Site LiDAR changes in snow depth with hourglass in situ transect overlaid. b) : In situ-measured vs. 10 m radius mean LiDAR-derived changes in snow depth.	18
2.6	a) : North Park Area, DeLine Site LiDAR changes in snow depth with hourglass in situ transect overlaid. b) : In situ-measured vs. 10 m radius mean LiDAR-derived changes in snow depth. The dark area toward the bottom of the site is the edge of the LiDAR survey.	19
2.7	a) : Gould Area, Whistling Elk Site LiDAR changes in snow depth with hourglass in situ transect overlaid. b) : In situ-measured vs. 10 m radius mean LiDAR-derived changes in snow depth. Again, the dark area toward the bottom of the site is the edge of the LiDAR survey.	20

2.8	a) : Oak Creek Area, Brenner Site LiDAR changes in snow depth with hourglass in situ transect overlaid. b) : In situ-measured vs. 10 m radius mean LiDAR-derived changes in snow depth.	21
2.9	a) : Rabbit Ears Area, Dumont Lake Site LiDAR changes in snow depth with hourglass in situ transect overlaid. b) : In situ-measured vs. 10 m radius mean LiDAR-derived changes in snow depth.	22
3.1	SNODAS estimates of snow depth change from December 3 rd , 2006 – February 22 nd , 2007.	30
3.2	SNODAS estimates of snow water equivalent on February 22 nd , 2007.	31
3.3	SNODAS estimates of total snow melt as a percentage of total snow precipitation from December 3 rd , 2006 – February 22 nd , 2007.	31
3.4	a) The SNODAS-estimated change in snow depth from Dec. 3 rd , 2006 – Feb. 22 nd , 2007 at all twelve sites from two CLPX-II Intensive Observation Periods. b) The difference between the SNODAS estimation and mean manual measurement as a function of measured depth at the same twelve hourglass sites.	32
3.5	Mean LiDAR-derived 5-meter snow accumulation value [cm] within each SNODAS 30 arc-second pixel from December 3 rd , 2006 – February 22 nd , 2007.	33
3.6	Mean LiDAR-derived 5-meter elevations [m] within each SNODAS 30 arc-second pixel.	34
3.7	LiDAR-derived vegetation density as a percentage within each SNODAS 30 arc-second pixel.	34

3.8	SNODAS depth change plotted against median LiDAR depth change within each 30 arc-second SNODAS pixel	36
3.9	Pixel by pixel SNODAS-LiDAR differences of snow depth change plotted against the mean LiDAR depth change within each SNODAS pixel. Three distinct regions are circled that fall outside the uncertainty of the LiDAR observations, signifying a particular physiographic forcing factor present in the three specific areas.	37
3.10	Pixel by pixel SNODAS-LiDAR differences of changes in snow depths. Hot colors are where SNODAS estimated a larger change in snow depth, while cold colors show where LiDAR observed a larger change.	39
3.11	Locations of wind redistribution model study areas just north of U.S. Highway 40 in Northern Colorado. The entire area was surveyed by the CLPX-II LiDAR, but during CLPX-I only the Walton Creek site received LiDAR acquisitions. Also during CLPX-II the Dumont Lake site was the subject of an intensive ground measurement campaign. .	44
3.12	Two sample wind DEM profiles. a) shows a case with a high terrain break (Sb) angle, while b) has a much lower terrain break value. . . .	46
3.13	Wind rose of Walton Creek meteorological station from September 2002 – May 2003. Only depicted are measurements of wind speeds capable of lifting and redistributing snow (Li and Pomeroy, 1997). An overwhelming majority of these high winds came from the due west direction.	48
3.14	Walton Creek maximum upwind slope parameter, S_x (in degrees), from 5-meter DEM using the 270° upwind direction and $d_{max} = 150m$. . .	49

3.15	Walton Creek terrain-break parameter, S_b (in degrees), from 5-meter DEM using 270° upwind direction, local $d_{max} = 50m$ and outlying $d_{max} = 150m$	49
3.16	LiDAR-derived, 5-meter resolution snow accumulation between December 3 rd , 2006 and February 22 nd , 2007.	50
3.17	LiDAR-derived, 5-meter resolution snow depths at Walton Creek as of December 3 rd , 2006.	51
3.18	Snow depths at Walton Creek as of February 22 nd , 2007.	51
3.19	Snow depths at Walton Creek as of April 9 th , 2003.	52
3.20	Statistically-determined drift and scour locations at the Walton Creek study area from three separate winter LiDAR acquisitions.	53
3.21	Histograms of snow depth after applied classification scheme for each ‘Snow-On’ LiDAR survey. Classification separates the persistently drifted and scoured pixels (extreme values) from other values that remain nearer to the mean of each survey.	54
3.22	Probability density functions of S_b and S_x at Walton Creek for known drift and scour cells from interannual consistency study.	56
3.23	LiDAR-observed changes in snow depth at Dumont Lake study area for December 3 rd , 2006 – February 22 nd , 2007. The lake can be seen in the northeastern corner.	57
3.24	Regions from the Dumont Lake LiDAR-derived change in snow depth raster where the terrain break parameter $S_b \geq -0.4^\circ$, and the maximum upwind slope parameter $S_x > 3.4^\circ$	58

3.25	Regions from the Dumont Lake LiDAR-derived change in snow depth raster where the maximum upwind slope parameter $S_x < 3.4^\circ$	58
4.1	Locations of time-lapse snow depth cameras in Idaho, USA	64
4.2	Bogus Basin study site layout showing location of the time-lapse camera with field-of-view and snow depth markers as well as snow pits and upward-looking radar. Snow-free (brown) and snow-covered (white) 20 cm digital surface models were obtained from repeated terrestrial laser scans.	65
4.3	Typical time-lapse snow depth camera system arrangement. dT , dG and h are measured and pixel size as a function of distance is predetermined, permitting the calculation of snow depth, Q , for every hourly image.	67
4.4	Sample images captured by the Bogus Basin study site camera with calculated snow depths displayed for both markers. Upper image was taken the day of installation.	68
4.5	Pixel-picking process of SnowDepthCam depth measurement. The thick red line in (a) represents the approximate measurement uncertainty. 70	
4.6	a) : Winter 2012-13 snow depth accumulation measured by three devices. Red and blue circles represent the near and far depth markers observed by the camera, green circles represent the SNOTEL ultrasonic sensor, and the black circles are the Boise State Hydrology Group ultrasonic sensor. b) : Close-up plot showing terrestrial LiDAR snow depth measurements at each marker as red and blue stars.	72

4.7	Plot of snow depth distribution at the Bogus Basin snow study site obtained by differencing two 20 cm Terrestrial LiDAR-derived DEMs. Time-lapse camera location is shown along with the field-of-view and snow depth markers #1 & #2. Negative snow depth values are due to multiple scan co-registration errors and interpolation edge effects from the LiDAR point cloud.	73
-----	--	----

CHAPTER 1:

INTRODUCTION

For millennia, the survival of human civilizations relied on the natural water cycle, but relatively recent advancements in irrigation and storage technology have permitted new settlements to abound within harsh, dry climates. Consequently, millions of people depend on diverted water from mountain snowpacks, resulting in an increased importance of observing and predicting the year-to-year magnitude of water stored in the seasonal snowpack, termed the snow water equivalent (SWE). In fact, studies have estimated that as much as one-sixth to over one-third of Earth's population relies on water that was previously stored as ice or snow upstream (Barnett *et al.*, 2005; Beniston *et al.*, 2003), further illustrating the importance of SWE forecasts by hydrologists and water managers during winter months.

The first step for developing accurate forecasts of mountain snowpacks is to analyze historical observations, which have been painstakingly maintained by various agencies for the past 50–75 years. Automated measurement stations are sparsely located over vast mountain regions at index sites, but do not resolve the actual spatial distribution and interpolation between sites is not possible. In spite of this fact, hydrologists have made very good use of the resulting rich temporal datasets by developing and distributing operationally viable prediction models of snowfall and snowmelt over very large areas using various statistical methods. While these forecasts are often satisfactory for streamflow forecasting on average years, they are highly uncertain in a changing climate and higher resolution spatial measurements are re-

quired to capture the hillslope- and micro-scale processes that can considerably affect snow distribution.

New advances in remote sensing technology are enabling measurements at spatiotemporal scales never before considered. Additionally, newly developed modeling techniques are taking advantage of higher resolution data to produce much better SWE estimates than ever before. This work synthesizes manual ground-based snow measurements, remote sensing observations, and model predictions in order to better quantify spatial and temporal variability in mountain snowpacks. Also addressed are the factors driving uncertainty in both remote sensing techniques and model estimates. The study is divided into three parts.

Part 1: Verifying measurements of snow depth with Light Detection and Ranging (LiDAR) using in situ manual measurements

Previous studies have shown that repeated, multi-temporal Light Detection and Ranging (LiDAR) acquisitions are a viable, albeit very costly and operationally intensive, method for obtaining high resolution snow depth information over large areas. However, with survey costs rapidly decreasing, the technology is sure to be an important component of future research of the seasonal snowpack. By performing one LiDAR survey over a snow-free landscape, then another once the ground is snow-covered, researchers can take a difference of the two surfaces to determine snow depths at the resolution of the original interpolated LiDAR elevation data.

LiDAR exhibits a certain amount of measurement uncertainty, as is the case with any measurement technique. One way to constrain this uncertainty is to perform ground-truth validation measurements during each acquisition to determine any bias

present in the dataset due to elevation, slope, aspect, point cloud density, and vegetation density. Taking this into consideration, Chapter 2 details a performance analysis of a large-scale LiDAR-derived snow accumulation dataset by comparing with coincident in situ manual measurements. Previous studies have necessarily upscaled the manual measurement information to the resolution of the obtained remote sensing data using various summary statistics (Yueh *et al.*, 2009) resulting in a modest number of well characterized locations for comparison, as many applications require average values at the 500 m to km scale. However, the LiDAR-derived snow depth data is at a sufficiently high resolution that a direct comparison can reasonably be made to each individual in situ depth measurement, resulting in a large number of data comparison points. This statistical comparison reveals information about the uncertainty present in the LiDAR snow depth dataset.

Part 2: Using LiDAR to validate SNODAS and a hydrologic wind redistribution model

Once the uncertainty of LiDAR snow depth change is quantified using ground-based measurements, we employ the high resolution depth information to validate a physically-based operational hydrologic model in Chapter 3. The SNOW Data Assimilation System (SNODAS) modeling framework operated by NOAA's National Hydrologic Remote Sensing Center (NOHRSC) produces daily predictions of snow depth and SWE at 30 arc second (effectively $1km^2$) resolution over the continental United States. Since both of the LiDAR acquisitions occurred early in the winter season well before the seasonal maximum snow water equivalent, the assumption is made that minimal melt occurred over the surveyed area thus allowing this work to focus solely on the

accumulation aspect of SNODAS. The median of the LiDAR-derived snow depths within pixels of archived concurrent SNODAS predictions are used to make a statistical comparison to assess the model performance for various degrees of terrain complexity and vegetation density.

At the smaller scale, wind redistribution is an important factor influencing local spatial variability of snow. Winstral and Marks (2002) presented an algorithm that calculates terrain-break parameters as a first step in developing scaled precipitation factors for corresponding pixels of an input DEM with known prevailing wind directions. Previous studies used 10–30 meter DEMs to accurately quantify wind’s effect on snow distribution in mountain catchments (Winstral *et al.*, 2009). For this study, using higher-resolution LiDAR DEMs, the wind model is executed for a $2km^2$ study area within the CLPX-II LiDAR footprint known to exhibit high sustained winter winds and preferential snow distributions that consist of large drifts up to 400% deeper than the surrounding snow.

Part 3: Time-lapse cameras for monitoring snow accumulation and ablation

Lastly, Chapter 4 addresses the need for higher resolution spatial *and* temporal observations unachievable by standard SNOTEL stations, SNODAS model output, or infrequent LiDAR, by presenting a low-cost and low-power method to measure hourly changes in snow depths at multiple locations at the slope scale over entire winter seasons. Using simple time-lapse photography and image processing, this technique provides a new way to obtain multiple hourly snow depth measurements at the slope scale. While this approach is no substitute for the spatial resolution of repeated ter-

restrial laser scans or the proven reliability of manufactured ultrasonic depth sensors, its low cost and automation make it a suitable method for monitoring networks of distributed snow depths.

CHAPTER 2:

CONSTRAINING LIDAR UNCERTAINTY WITH IN SITU MANUAL MEASUREMENTS

2.1 Summary

Utilizing large-scale multi-temporal LiDAR (Light Detection And Ranging) surveys, we can develop high resolution snapshots of mountain snow distributions at distinct moments during accumulation and ablation periods. As with any remote sensing method, LiDAR exhibits a degree of measurement uncertainty, which is compounded by the need for multiple surveys to detect changes in snow depth. In situ manual snow depth measurements during “snow-on” surveys aid in limiting this uncertainty and can discover LiDAR measurement bias due to absolute positioning differences between flights, forest canopy cover, elevation gradients, and snow surface albedo or roughness.

We illustrate the importance of manual measurements for validating remote sensing data and constraining the absolute error of large-scale LiDAR surveys using statistical comparison techniques. Additionally, we present evidence of sampling shortcomings with uniform manual measurement transects due to the high degree of variability present in mountain snowpacks.

2.2 Introduction

Modeling the Earth's surface terrain from recorded elevation data is a mature technique and has been vital to geoscientists since the first elevation model was produced. Over the last thirty years, 10–30 meter DEMs have been interpolated over much of the Earth from various sources such as cartographic contours, geological survey topographical data, and remote sensing satellites such as the Shuttle Radar Topography Mission (SRTM). However, increasing the resolution of the modeled Earth surface has required a new method to more accurately measure elevations at higher spatial resolutions.

Light Detection And Ranging (LiDAR) was initially developed in the early 1960's and was based on the same physics as sonar and radar sounding methods. Specifically, pulsed light waves exhibit substantially shorter wavelengths than sound- and micro-waves, allowing a more accurate measurement of distances from source to receiver. In the mid-1980's, the first Global Positioning System (GPS) satellites were deployed, enabling LiDAR scanners to be mounted on aircraft and produce large airborne surveys of the Earth's surface. With technological advances in optical sensors and exponentially larger data storage capacities, LiDAR sensors are now able to produce high resolution ($<1\text{--}5\text{m}$) DEMs over enormous geographic areas. Thus, when LiDAR is used to examine seasonal snowpacks, high resolution measurements of snow depth can be produced by simply subtracting the snow-free surface from the snow-covered surface.

To conduct an airborne LiDAR survey, laser pulses are transmitted from an aircraft and measurements are made of the time the pulses take to return to the receiving sensor after reflecting off ground-based objects. With an onboard high-precision GPS

system and Inertial Measurement Unit (IMU) to correct for the roll, pitch, and yaw onboard the aircraft, in addition to GPS base stations on the ground, the positions of pulse reflection locations can be determined to centimeter relative accuracy using differential GPS triangulation methods.

Each of these components introduces a noticeable amount of error into a LiDAR dataset for even the most ideally flat landscape with no vegetation. Error is further exacerbated when considering complex mountain terrain with high slope angles and dense forest canopy (Hodgson and Bresnahan, 2004). Furthermore, snow has a relatively high volumetric scattering component when compared to other terrain surfaces, resulting in a lower return intensity spectrum to the LiDAR receiver especially at steep grazing angles (Deems *et al.*, 2013). And lastly, the requirement of two separate scans for snow depth derivation can double snow depth measurement uncertainties to as much as 40-50 cm. The consideration of these uncertainty factors for remote sensing to capture spatial variability leads to the necessity of ground-based manual measurements for error quantification.

The first major LiDAR survey campaign for seasonal snow applications was carried out during the 2003 National Aeronautics and Space Administration (NASA) Cold Lands Processes Experiment (CLPX-I) in Colorado, USA. Nine 1x1 km Intensive Study Areas (ISAs) were chosen that represented various accumulation and ablation patterns (Cline *et al.*, 2009) ranging from heavily snow-covered prairies to high-alpine forests and wind-scoured cirques. Aerial LiDAR surveys were conducted over the ISA's at the approximate time of peak snow water equivalent in early April 2003 and then again over the same snow-free surface in September 2003 with average point spacings of about 1.5 meters. The LiDAR return point clouds from each survey were

then interpolated to grids of similar spatial extent and resolution, then differenced for a snow depth product over the extents of each ISA.

Previous studies of spatial variability using the CLPX-I LiDAR have shown that snow depth distributions display fractal behavior in their spatial patterns (Deems *et al.*, 2006; Trujillo *et al.*, 2007). Deems *et al.* (2008) used an additional April 2005 survey and showed that there exists an interannual consistency in the snow depth distribution at two of every ISA, while Trujillo *et al.* (2007) found that spatial distributions of snow depth are strongly controlled by both wind redistribution and vegetation interception of snow over uneven surface topography in five of the CLPX-I ISAs. The LiDAR data from the CLPX-I campaign is primarily presented in Chapter 3.

Three years later, a similar tactic was implemented for the CLPX-II campaign at a much larger scale, and the results of this second campaign are presented in this chapter. Two airborne LiDAR surveys were flown over a large swath of Northern Colorado in unison with coordinated in situ measurement campaigns on December 3rd, 2006 and February 22nd, 2007. The in situ snow surveys were designed by Kelly Elder of the USDA Forest Service Rocky Mountain Research Station and carried out by a large team of field researchers. Of particular note is that the December survey does not necessarily represent a “snow-free” survey as much of the area was already blanketed in snow. However, for this study, it will be treated as such and therefore any mention of LiDAR-derived snow depths from CLPX-II are actually the *change* in total snow depth between the two surveys. This is the first comparison between the LiDAR and in situ datasets of CLPX-II with the goal of determining a quantifiable uncertainty to the LiDAR-derived snow depths for further modeling applications.

2.3 Methods

2.3.1 Site Description

The second Cold Lands Processes Experiment (CLPX-II, 2006-2008) campaigns in Colorado and Alaska, USA were multi-faceted missions over a much larger scale than the previous CLPX-I campaign three years prior. The primary objective of the Colorado mission was the acquisition of snow volume backscatter measurements with NASA’s POLSCAT (POLarimetric SCATterometer) airborne Ku-band radar system and the necessary ground truth measurements for validation (Yueh *et al.*, 2009) of the proposed NASA SCLP and ESA CoreH2O approach to SWE estimation using microwave radar from space. The airborne LiDAR portion of the campaign was an ancillary dataset to be used as extra validation for the radar measurements. Flown onboard a separate aircraft, the LiDAR acquisitions were designed to cover a much larger geographic area than the CLPX-I ISAs and allow evaluation of the radar SWE inversion over a larger range of conditions than possible with manual ground-truth observations.

These large-scale LiDAR acquisition flights were conducted on December 3rd, 2006 and February 22nd, 2007 over a 750 km^2 rectangular area of northern Colorado (Figure 2.1). The average point spacing of the raw unfiltered point cloud delivered by the vendor was approximately 1.75–2.0 meters depending on the terrain, resulting in a slightly less dense dataset than the original CLPX-I acquisitions but covering many more types of terrain, vegetation, and snowpacks. The LiDAR flight vendor, Fugro Horizons, Inc., filtered vegetation returns from ground returns using a minimum block mean algorithm and proprietary software to create vegetation filtered point clouds for

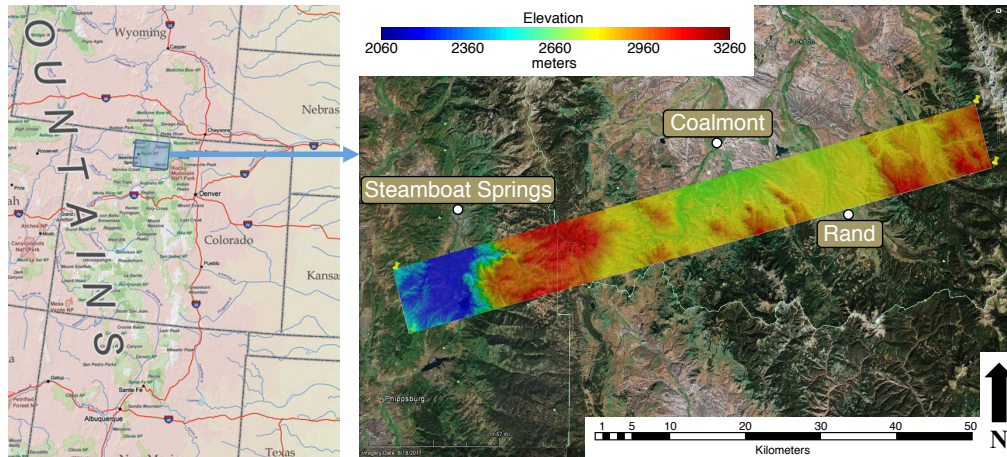


Figure 2.1: Location of CLPX-II LiDAR footprint in Northern Colorado, USA

each flight with nominal point spacings of 2.5–3.0 meters depending on the terrain and canopy cover. Various alternative filtering algorithms were explored during the research for this thesis, but the decision was ultimately made to utilize the vendor-filtered data in order to maintain consistency over the large variety of landscapes. Next, the open-source Points2Grid interpolation tool, employing an inverse distance weighting scheme, was used to produce a 5-meter Digital Elevation Model (DEM) of each survey and the surfaces were differenced to deliver the change in total snow height at 5-meter resolution between December 3rd and February 22nd (Figure 2.2). Finally, the vegetation-classified point clouds were also gridded for use in deriving canopy height at the same 5-meter resolution.

2.3.2 In Situ Measurements

To help constrain the LiDAR uncertainty, twelve intensive observation sites of distinct terrain and vegetation characteristics were pre-selected by researchers for in situ snow depth measurements during each LiDAR acquisition. At each site, 45–50 manual

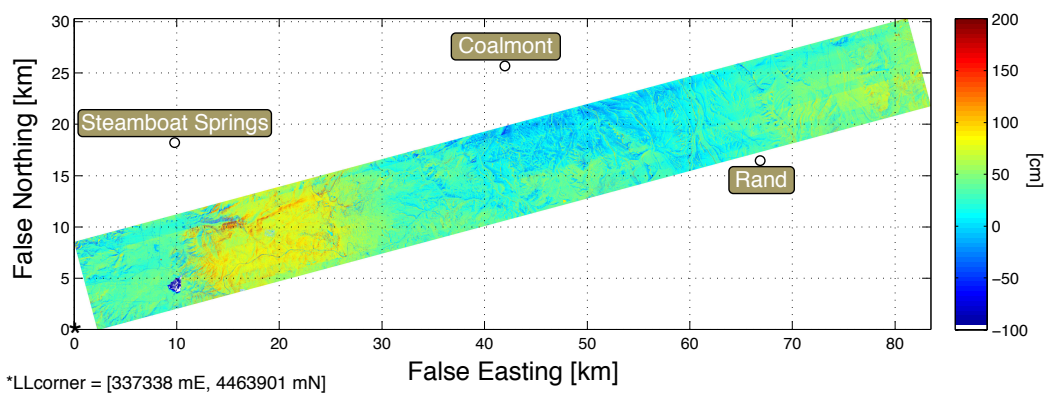


Figure 2.2: LiDAR-derived change in total snow depth at 5-meter resolution for the period of December 3rd, 2006 – February 22nd, 2007.

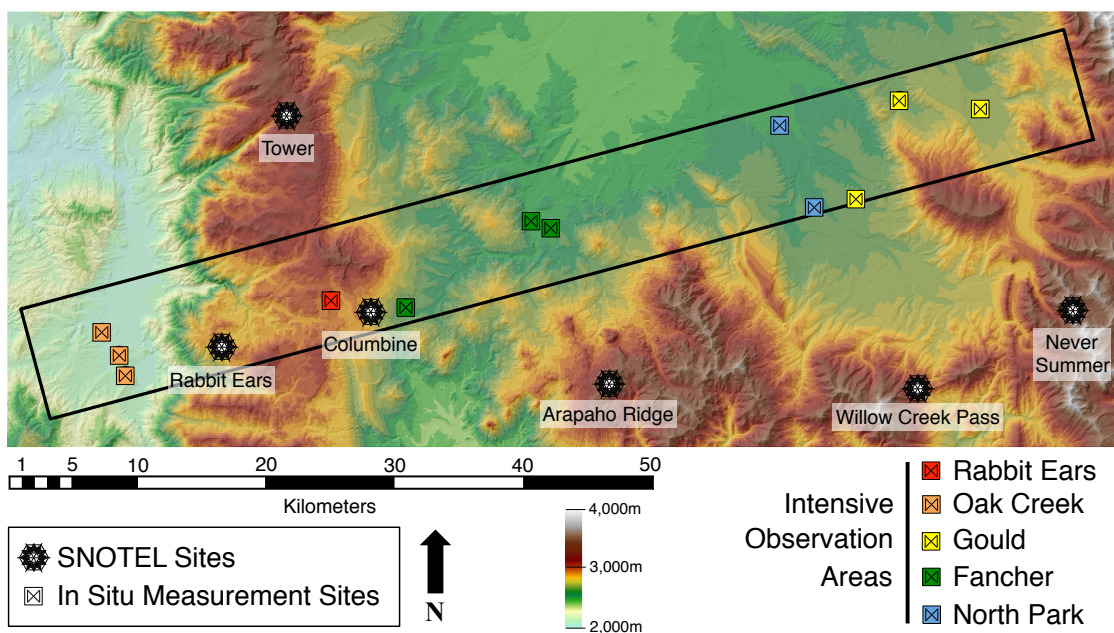


Figure 2.3: Locations of in situ intensive observation sites within CLPX2 LiDAR footprint. Also shown are the six nearest Snow Telemetry (SNOTEL) sites maintained by the Natural Resource Conservation Service (NRCS).

samples of depth were made along a 500 m \times 500 m hourglass-shaped transect to be used to quantify the error in the simultaneous LiDAR measurements. The locations of in situ measurement sites are shown in Figure 2.3.

Crews measured snow depths during both LiDAR surveys at waypoints loaded onto mapping grade handheld GPS units to maintain the hourglass shape chosen by the planning team. The resulting relative point-to-point horizontal uncertainty is estimated to be less than 2 meters while the hourglass transect locations can be approximated to 7 meters in absolute space (K. Elder, personal communication).

The sites were classified into broad study areas depending on varying elevations, mean snow depths, terrain features and vegetation characteristics. Intensive measurement sites were organized into larger encompassing areas representative of similar environmental features (Table 2.1). To capture the horizontal uncertainty in both the in situ measurements and LiDAR-interpolated snow depths, LiDAR depths were averaged in a 10 meter radius around the reported in situ measurement location. Vegetation was also considered by utilizing the filtered non-ground point cloud returns and creating a new gridded canopy surface at 5-meter resolution. Cells were classified as having vegetation if the difference between the snow-free DEM and vegetation digital terrain model (DTM) was greater than 50 cm, resulting in a vegetation density map for the entire CLPX-II survey footprint.

Table 2.1: Site descriptions for CLPX-II Intensive Observation Periods

Area	Site	Mean Accumulation [cm]		Vegetation Density [%]	Description
		In situ	Lidar		
Fancher	Arapahoe	16	9	11	[2550 – 2650 m.s.l.] Flat, open rangeland; dense low-lying vegetation (sagebrush); occasional tree stands (willow, cottonwood); frequent high winds; located in rain shadow east of the Park Range
	C-Van	22	19	28	
	Spicer	55	42	15	
North Park	Illinois River	19	9	9	[2550 – 2600 m.s.l.] Flat, grass-covered rangeland; scattered bushes 3-5 meters tall; heavy wind-scouring resulting in low snow accumulation
	DeLine	28	16	7	
Gould	Whistling Elk	32	26	6	[2550 – 2600 m.s.l.] Rolling farmland; scattered coniferous forests; higher snowfall totals; located at western base of the Medicine Bow Mountains
	Silver Spur	43	33	47	
	Baller	53	49	25	
Oak Creek	Lake Catamount	47	39	12	[2100 – 2150 m.s.l.] Rolling farm & ranch land spotted with grasses and small shrubs; comparatively low elevations; located at western base of the Park Range
	Sydney Peak	48	32	5	
	Brenner	64	42	3	
Rabbit Ears	Dumont Lake	97	73	26	[2900 – 2950 m.s.l.] Undulating, complex terrain; scattered coniferous groves; very high snow totals; persistent wind redistribution of snow; drifts up to 5 meters deep

2.4 Results

Comparisons of five intensive observation sites, each representing a different designated area, are shown in Figures 2.5 – 2.9.¹ The images of the in situ hourglass transects overlaid upon the LiDAR-derived snow depths illustrate the difficulty of manually sampling the scale of complexity present in mountain snow distributions. On the other hand, the scatter plots reveal that the LiDAR-derived snow depths routinely underestimate corresponding measurements made by the fixed position probe transects. For the twelve in situ measurement transects, the LiDAR-derived depth dataset underestimated manual measurements by 5–30 cm. By comparing the mean in situ-measured and LiDAR-derived snow depth change within each site (Figure 2.4), the underestimation offset of the LiDAR dataset is quickly apparent; however, the two estimates are highly correlated and the RMS difference of 12 cm is well within the expected LiDAR uncertainty.

Located in a flat, heavily wind-scoured region, which only saw very slight accumulation totals between survey dates, the Arapahoe site (Figure 2.5) demonstrated a very low correlation between in situ and LiDAR measurements. This can be explained by the fact that the mean in situ depth change measurement is well within the accepted uncertainty of airborne LiDAR. Yet, this error is certainly compounded by the tendency of uniform in situ measurement transects to bypass large accumulation areas that are observed by LiDAR. Figure 2.5b shows that the LiDAR interpolations observed negative changes in snow depth between the two flights, which the manual transects did not.

¹Most literature estimates the uncertainty of multi-temporal LiDAR change-detection surveys to approximately 30 centimeters. Therefore, the pink squares on each site scatter plot display the magnitude of approximate LiDAR error in relation to the range of in situ snow depths.

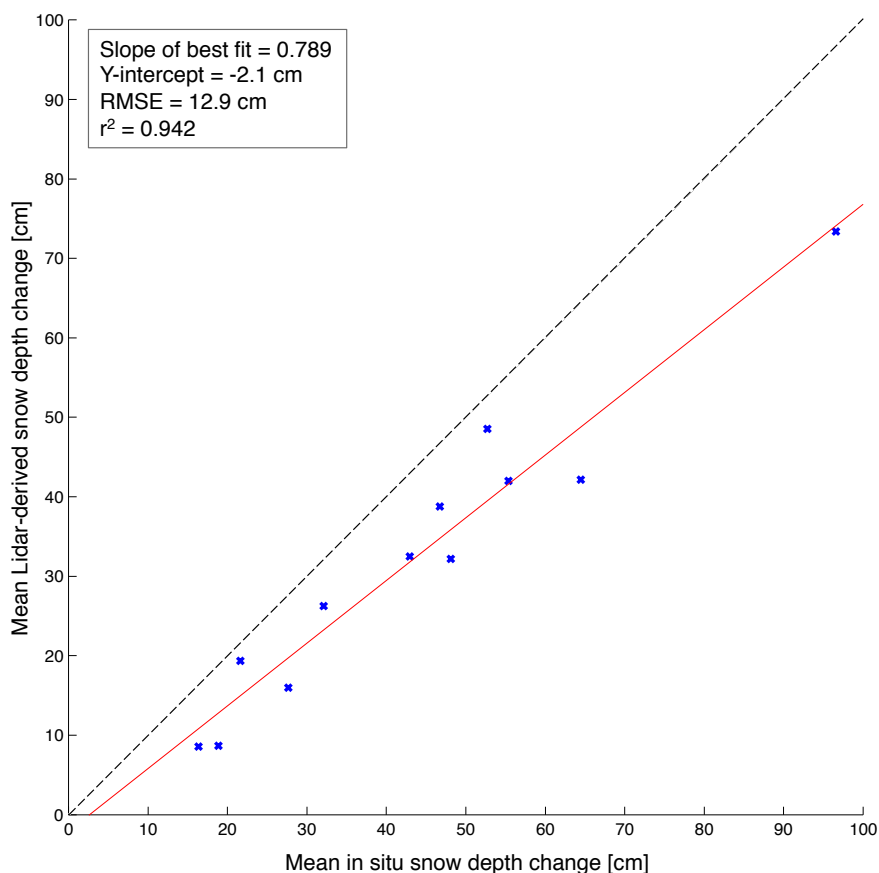


Figure 2.4: Comparison of mean LiDAR-derived vs. mean in situ-measured snow depth change (Dec. 3rd – Feb. 22nd) over each of the twelve Intensive Observation Period sites.

The DeLine site (Figure 2.6) in the North Park area, with a slightly higher mean snow total, displayed a higher correlation between the manual and remote measurements. The landscape of this site is largely similar to the Arapahoe site with flat terrain and low, dense sagebrush mostly lower than 50 cm tall.

Next, within the Gould area lies the Whistling Elk site (Figure 2.7) which presented the highest correlation between LiDAR and manual measurements. This site is also substantially bare of vegetation and displays barely any terrain undulation.

These factors likely explain the high correlation.

The Brenner site (Figure 2.8) within the Oak Creek area to the far western end of the CLPX-II LiDAR swath is somewhat of an anomaly to the other twelve sites. The correlation between manual and remotely-observed changes in snow depth appears almost random, similar to the Arapahoe site, but the mean snow depth change is much higher. The image of LiDAR-derived snow depth change exhibits some drifting patterns and variability, but the manual measurements were consistently higher.

To the northwest of Rabbit Ears Pass along U.S. Highway 40 lies the Dumont Lake intensive site (Figure 2.9). Situated just 1 km east of the Walton Creek study site from the CLPX-I campaign, the site displays a great deal of variability in the form of large accumulation areas due to nearly constant west to east winter winds. A much higher correlation value exists between the LiDAR and in situ measurements at the site, but the root-mean-square difference between the datasets is much higher due to the larger range of changes in snow depth throughout. This site will be revisited in Chapter 3 for a more comprehensive study.

Area: Fancher Site: Arapahoe

Elevation = 2590 m
 Mean in situ depth change = 16 ± 14.5 cm
 Mean Lidar depth change = 9 ± 18 cm
 Vegetation Coverage = 11%
 RMSD = 19 cm
 $r^2 = 0.068$

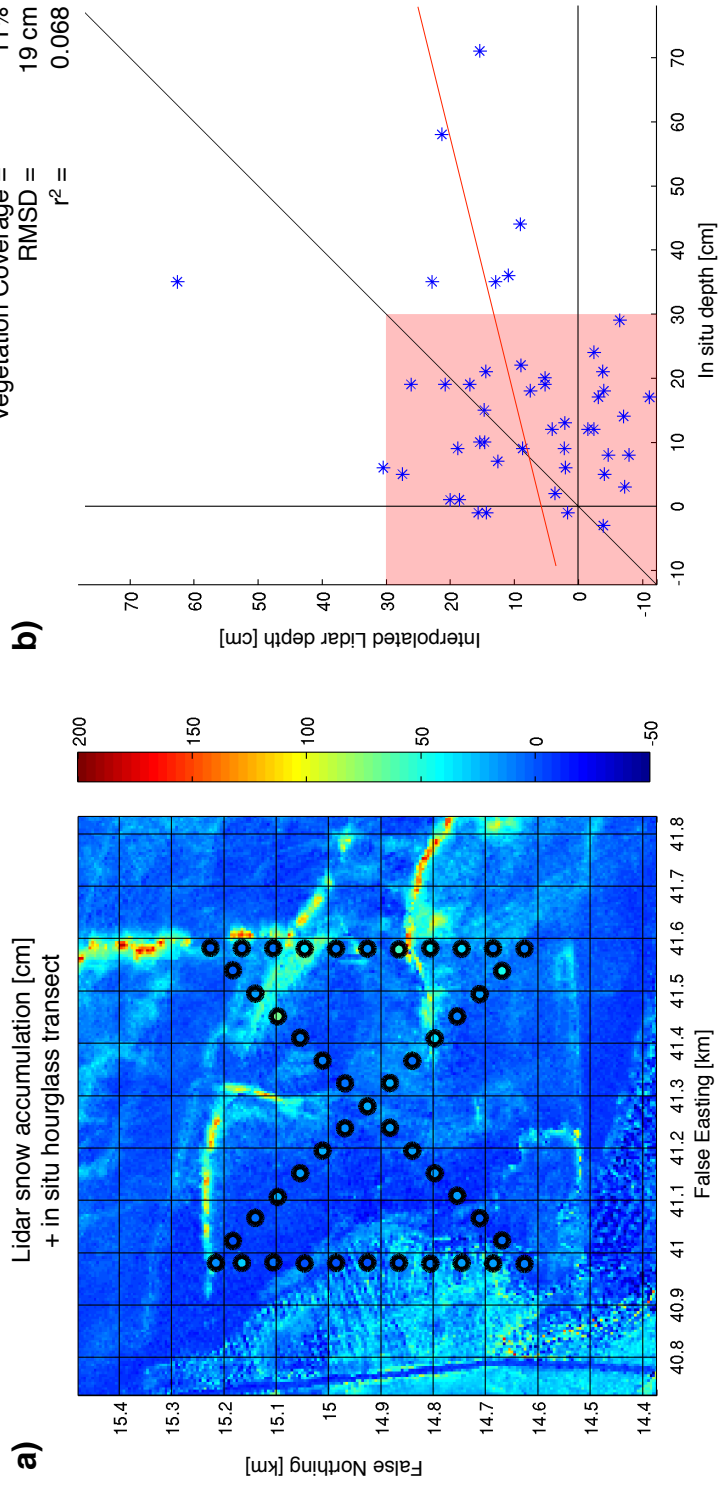


Figure 2.5: **a)** Fancher Area, Arapahoe Site LiDAR changes in snow depth with hourglass in situ transect overlaid. **b)** In situ-measured vs. 10 m radius mean LiDAR-derived changes in snow depth.

Area: North Park Site: DeLine

Elevation = 2610 m
 Mean in situ depth change = 28 ± 8.8 cm
 Mean Lidar depth change = 16 ± 4.8 cm
 Vegetation Coverage = 7%
 RMSD = 14 cm
 $r^2 = 0.496$

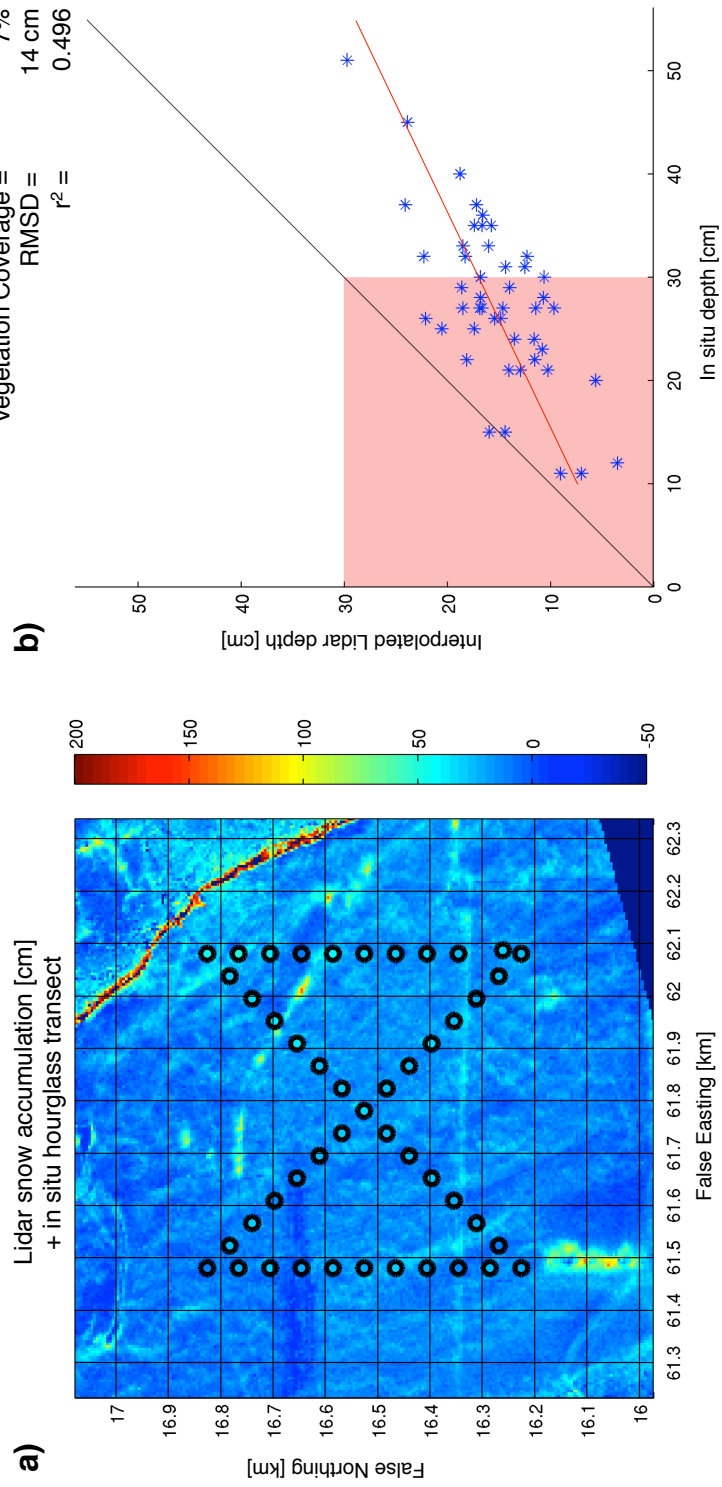


Figure 2.6: **a)** North Park Area, DeLine Site LiDAR changes in snow depth with hourglass in situ transect overlaid. **b)** In situ-measured vs. 10 m radius mean LiDAR-derived changes in snow depth. The dark area toward the bottom of the site is the edge of the LiDAR survey.

Area: Gould Site: Whistling Elk

Elevation = 2620 m
 Mean in situ depth change = 32 ± 15 cm
 Mean Lidar depth change = 26 ± 9 cm
 Vegetation Coverage = 6%
 RMSD = 11 cm
 $r^2 = 0.692$

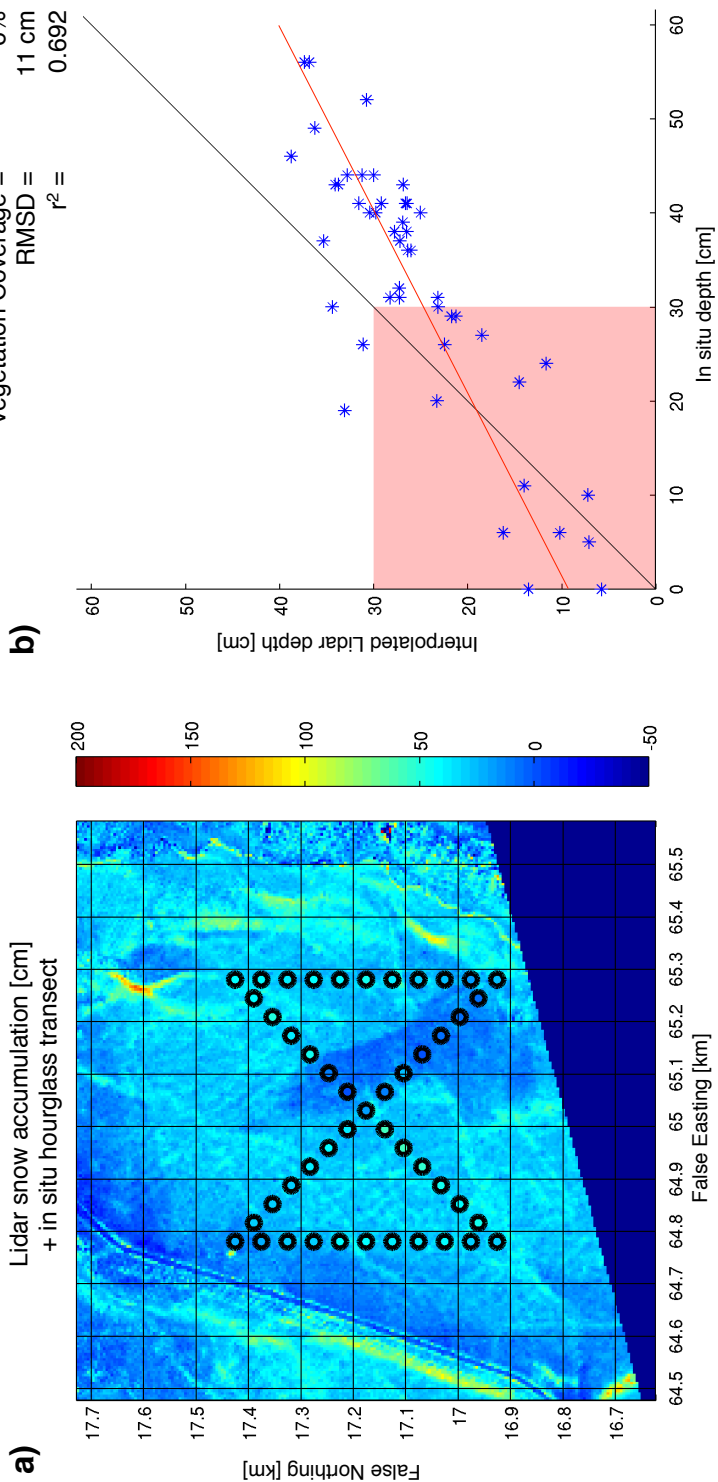


Figure 2.7: **a)** Gould Area, Whistling Elk Site LiDAR changes in snow depth with hourglass in situ transect overlaid. **b)** In situ-measured vs. 10 m radius mean LiDAR-derived changes in snow depth. Again, the dark area toward the bottom of the site is the edge of the LiDAR survey.

Area: Oak Creek Site: Brenner

Elevation = 2100 m
 Mean in situ depth change = 64 ± 13 cm
 Mean Lidar depth change = 42 ± 11 cm
 Vegetation Coverage = 3%
 RMSD = 26 cm
 $r^2 = 0.073$

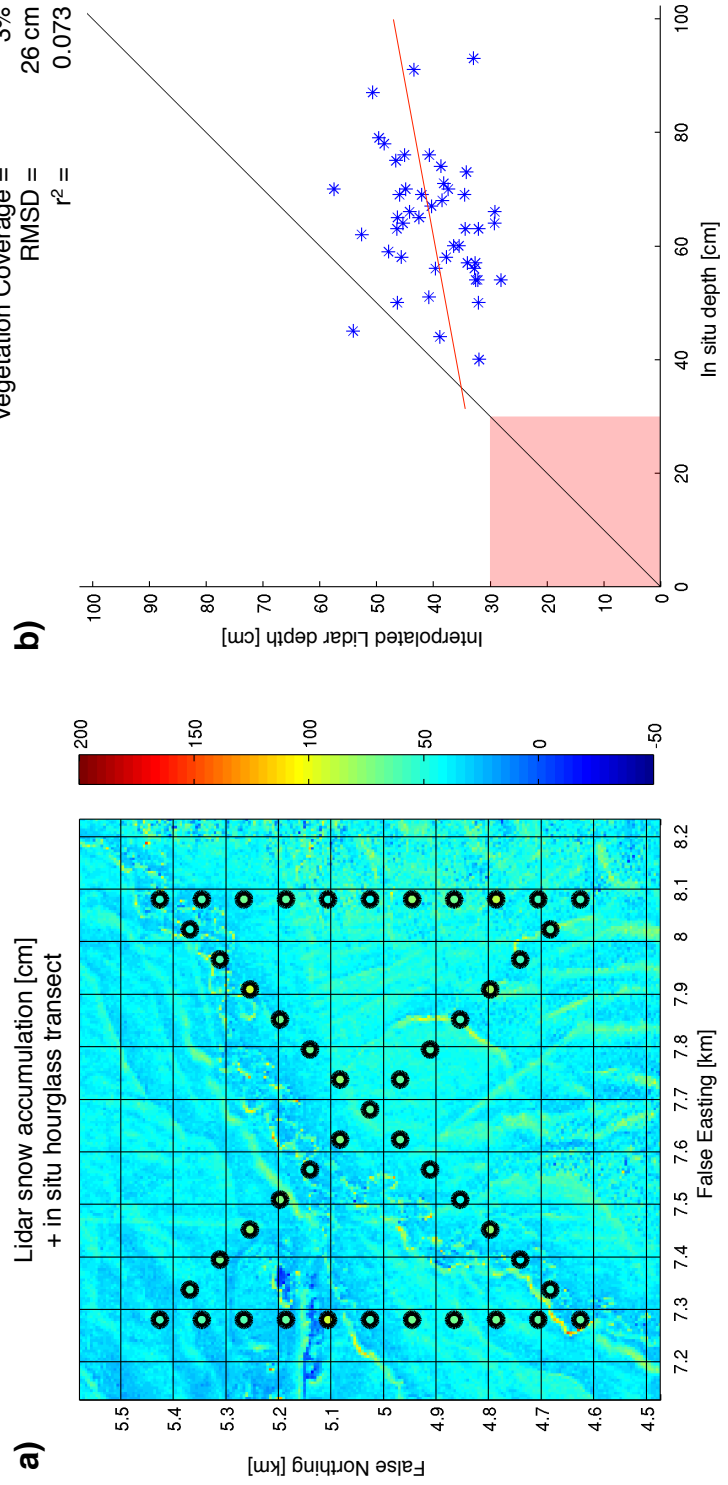


Figure 2.8: a): Oak Creek Area, Brenner Site LiDAR changes in snow depth with hourglass in situ transect overlaid. b): In situ-measured vs. 10 m radius mean LiDAR-derived changes in snow depth.

Area: Rabbit Ears Site: Dumont Lake

Elevation = 2930 m
 Mean in situ depth change = 97 ± 72 cm
 Mean Lidar depth change = 73 ± 40 cm
 Vegetation Coverage = 26%
 RMSD = 42 cm
 $r^2 = 0.496$

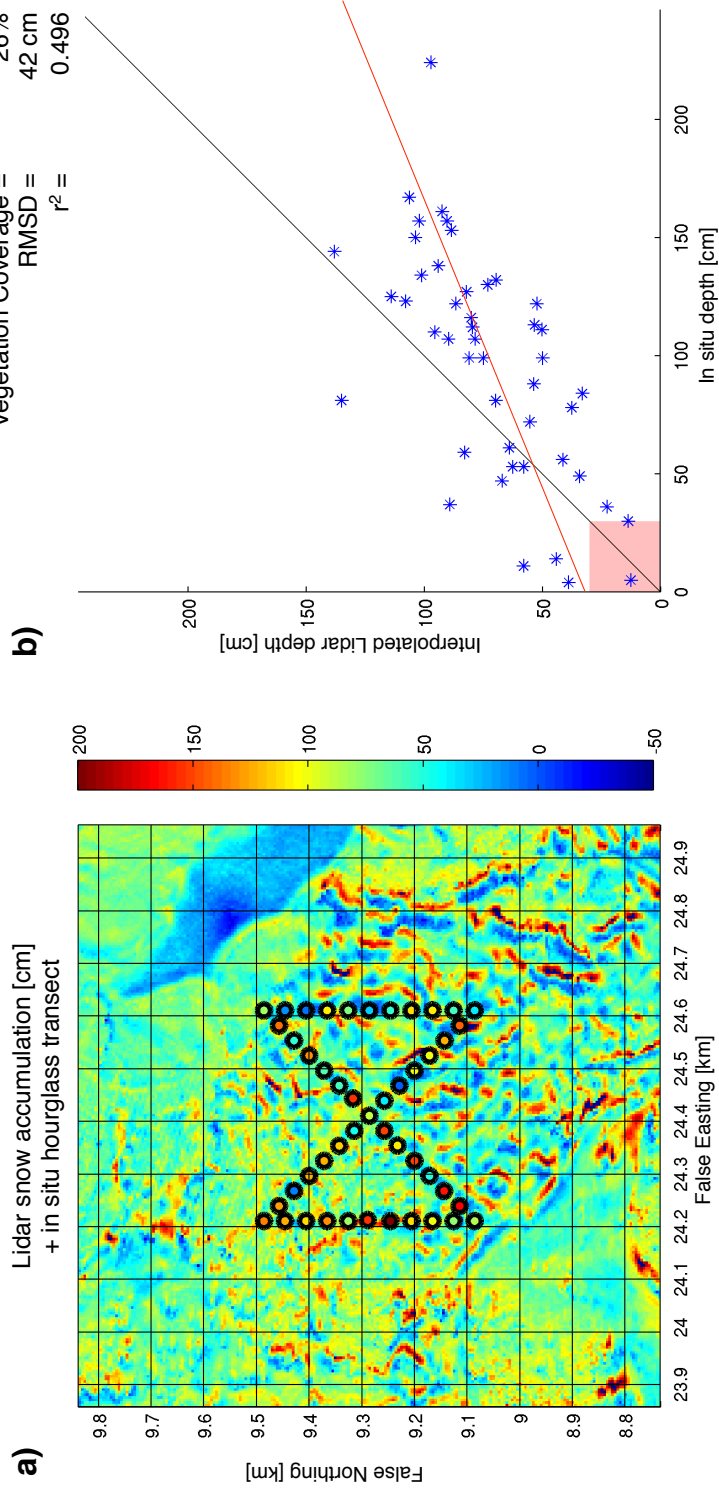


Figure 2.9: a): Rabbit Ears Area, Dumont Lake Site LiDAR changes in snow depth with hourglass in situ transect overlaid. b): In situ-measured vs. 10 m radius mean LiDAR-derived changes in snow depth.

2.5 Discussion

LiDAR is a helpful tool for those researching the seasonal snowpack, adding a vast amount of information about spatial variability that was previously very difficult to quantify with manual measurement surveys and snow courses. For water managers and snow hydrologists, however, it is important to have firm confidence in remote sensing data by constraining any absolute error sources. LiDAR vendors are primarily in charge of eliminating relative error sources stemming from swath overlap and GPS triangulation, but for snow applications the end-user is often responsible for understanding possible sources of absolute error within the survey footprint such as dense vegetation, steep slopes, and albedo effects. This can be accomplished by performing coincident manual measurement surveys during each LiDAR acquisition.

The exhaustive CLPX-II in situ measurement campaign provided an ideal dataset for limiting uncertainty in the large-scale LiDAR surveys of December 3rd, 2006 and February 22nd, 2007. Statistical comparisons found that LiDAR-derived snow depths were regularly 5–30 centimeters lower than the probe-measured snow depths, likely due to a variety of factors. One viable explanation would be the difference in measurement support between LiDAR and in situ measurements. Where the manual depth measurement support was less than a centimeter (the size of the depth probe tip), the LiDAR-derived snow depth change was averaged over all the 5-meter pixels within a 10-meter radius of the reported in situ measurement location. This smoothing of the snow height change would naturally result in a lower value than the point measurement.

On the other hand, the high resolution LiDAR data reveals the extent of variability that goes without being sampled by standard manual measurement transects in

complex terrain. A plausible solution for eliminating absolute error within a LiDAR-derived snow depth dataset would be to add a vertical shift determined by the intensive manual measurement comparison, and then to trust the observed relative spatial variability to be representative of the actual snow distribution.

Other sources of uncertainty include vegetation filtering and absolute positioning. Manual observations have uncertainties related to absolute positioning and measurement error due to the probe penetrating the soil or not reaching the ground due to ice layers. We believe the most likely source of differences between LiDAR and manual observations are due to the differences in support, geolocation errors, and vegetation filtering / LiDAR penetration in dense vegetation and shallow snowpacks.

CHAPTER 3:

USING LIDAR SNOW DEPTH INFORMATION TO VALIDATE SNODAS AND FORCE A WIND REDISTRIBUTION MODEL

3.1 Summary

Using CLPX-II LiDAR-derived snow depth information over complex mountain terrain, we explore the ability of the SNODAS operational hydrologic model to predict and update snow depth values between LiDAR acquisitions. We upscale high resolution LiDAR-derived changes in snow depth to the spatial resolution of daily SNODAS estimates while assuming that no ablation occurred over the study area between LiDAR flights, in order to compare a robust dataset of more than 900 coincident pixels of measured and modeled data for various elevations, terrain types, and vegetation densities. Then, we turn to a hydrologic wind redistribution model to develop a tool for determining sub-kilometer variability over large geographic areas. Using high resolution elevation data, we execute the wind model at two sites within the LiDAR swath to calculate terrain parameters based on the maximum upwind slope. At each site, the distribution of model terrain parameters reveals evidence of spatial trends with the drifting and scouring patterns observed by repeated LiDAR surveys.

3.2 Validating SNODAS

3.2.1 Introduction

Each year water managers and snow hydrologists use various hydrologic models to make important predictions of the amount of water stored in mountain snowpacks based on myriad forcing factors. Model input sources include the network of SNOw TELEmetry (SNOTEL) stations, weather forecasts, global climate models, and satellite imagery of snow covered area. These predictions of snow water equivalent are vitally important to downstream communities that rely on snow melt to subsist. The SNOw Data Assimilation System (SNODAS), developed and operated by the National Weather Service's National Operational Hydrologic Remote Sensing Center (NOHRSC), is updated each day at 30 arc-second (nominally $1km^2$) resolution to provide a tool for water managers to plan for surpluses and shortages in the water supply, energy production, fish habitat maintenance, and flood mitigation.

The SNOw Data Assimilation System

First implemented in 2004, SNODAS estimates various snow properties by merging satellite, airborne, and ground-based snow data with modeled approximations of snow cover (Barrett, 2003). The physically-based energy- and mass-balance NOHRSC Snow Model is the primary component of SNODAS, but the assimilation step gives analysts the ability to decide every day whether to augment the model estimates with any available remote sensing or SNOTEL measurements. Ultimately, the downscaled products have a spatial resolution of 30 arc-seconds (nominally $\approx 1km^2$) over the contiguous United States. The National Snow and Ice Data Center (NSIDC) archives

and makes daily estimates available to the public of:

1. Snow water equivalent (SWE)
2. Snow depth
3. Snow melt runoff from the base of the snowpack
4. Sublimation from the snowpack
5. Sublimation of blowing snow
6. Solid precipitation
7. Liquid precipitation
8. Snowpack average temperature

Only the first and second SNODAS daily estimates (SWE and snow depth) are examined with this comparison study. This is because the February LiDAR survey that produced the observations of snow depth change occurred well before the date of annual maximum SWE and the start of the primary melt season.

The special report describing the SNODAS data assimilation scheme and the available products (Barrett, 2003) mentions a noticeable lack of objective validation of SNODAS simply due to the fact that effectively all available automated remote sensing and ground-based data is inherently assimilated into the model framework. However, independent studies are the only method for obtaining impartial comparison metrics to properly validate SNODAS. As of 2013, only two studies have focused on validation of SNODAS using external independent datasets.

The first study by Anderson (2011) consisted of a comparison and validation study over two winter seasons after taking thousands of depth measurements with a Snow Magnaprobe and hundreds of SWE measurements using a Federal Snow Sampler just to the north of Boise, Idaho in the Dry Creek Experimental Watershed. Results concluded that SNODAS under-predicted both SWE and depth within the three study pixels most likely due to sub-kilometer spatial variability that cannot be considered by the modeling framework, and due to the sites having a predominantly southern aspect, while the nearest SNOTEL station is sheltered by a nearby north facing slope.

Then, Clow *et al.* (2012) used 45 ground-based snow survey transects located around the state of Colorado and within separate SNODAS pixels to study the SWE and snow depth estimation ability of the model. Their findings found that the model framework performs well in the sampled forested regions, but underestimates SWE and depth in leeward (wind-sheltered) alpine terrain while overestimating in windward-sloping (scoured) areas.

Thus, for the first time, a dataset of large spatial extent is used to analyze the effectiveness of SNODAS in estimating changes in snow depths during the accumulation season. The CLPX-II 750 km² LiDAR acquisitions sampled snow depths over a wide span of elevations (2070–3260 m.s.l.), slopes, and vegetation types while covering 980 individual SNODAS pixels, providing a large database of comparisons between measurements and model estimates.

As mentioned previously, this study primarily evaluates SNODAS for accumulation events by the assumption that a negligible amount of snowmelt occurred between December 3rd, 2006 and February 22nd, 2007 — the dates of each CLPX-II airborne LiDAR survey. Also, by December 3rd, many locations within the survey area had

received a perceptible amount of snow. Therefore, the difference between the bare-Earth surfaces of each survey date represents only the change in snow height and does not take into account any changes in depth due to ablation or sublimation that occurred between the flight dates. Since the LiDAR depth change is compared to the SNODAS depth change, this should not be an issue even if there was significant ablation, or sublimation. However, as these components of the mass balance were likely small, this study primarily evaluates the accumulation and densification components of SNODAS.

3.2.2 Methods

The second Cold Lands Processes Experiment (CLPX-II), as previously described, was conducted over the 2006-07 winter season and was designed primarily to validate the ability of the airborne POLSCAT (Polarimetric Scatterometer) sensor to measure radar backscatter components from the snowpack for SWE estimation. Flown in conjunction with two of the POLSCAT acquisitions and manual measurement campaigns described in Chapter 2, the CLPX-II LiDAR was intended to be a radar instrument validation dataset by supplying direct measurements of snow height changes at high spatial resolutions.

SNODAS estimates of SWE and depth were downloaded from the National Snow and Ice Data Center (NSIDC) for the two dates of the LiDAR acquisitions, then converted to raster form and spatially referenced to the UTM coordinate projection using ArcGrid software. The resulting estimate of the snow height change between December 2006 and February 2007 is shown in Figure 3.1 along with the boundary of the coincident LiDAR surveys as well as all nearby SNOTEL stations. Figure 3.2

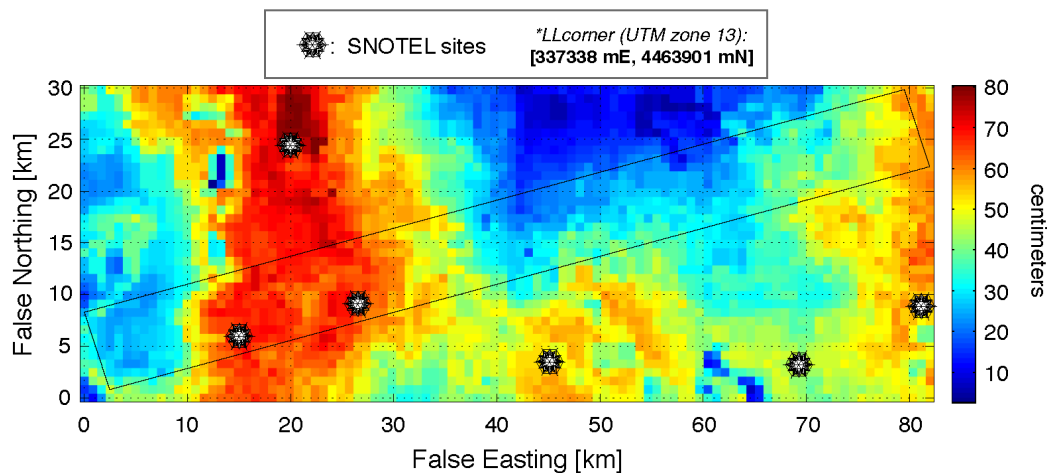


Figure 3.1: SNODAS estimates of snow depth change from December 3rd, 2006 – February 22nd, 2007.

then displays the model estimated snow water equivalent present in the vicinity of the LiDAR footprint on February 22nd, 2007. The SNODAS daily estimated snow melt between LiDAR acquisitions was then summed to bolster the assumption that minimal melt occurred over the study region. Figure 3.3 shows that only in the North Park region 10–20% of the total snow precipitation was estimated to have melted away due to solar radiation and air temperature. Everywhere else within the survey swath experienced a negligible percentage of snow melt.

3.2.3 Results

The manual measurement campaign detailed in the preceding chapter produced twelve hourglass snow depth measurement sites over a wide range of physiographically distinctive areas. The mean measured change in snow depth at each site was found with an associated interquartile range, similar to Clow *et al.* (2012). Then, a coincident 30 arc-second pixel estimate of depth change was created over each hourglass

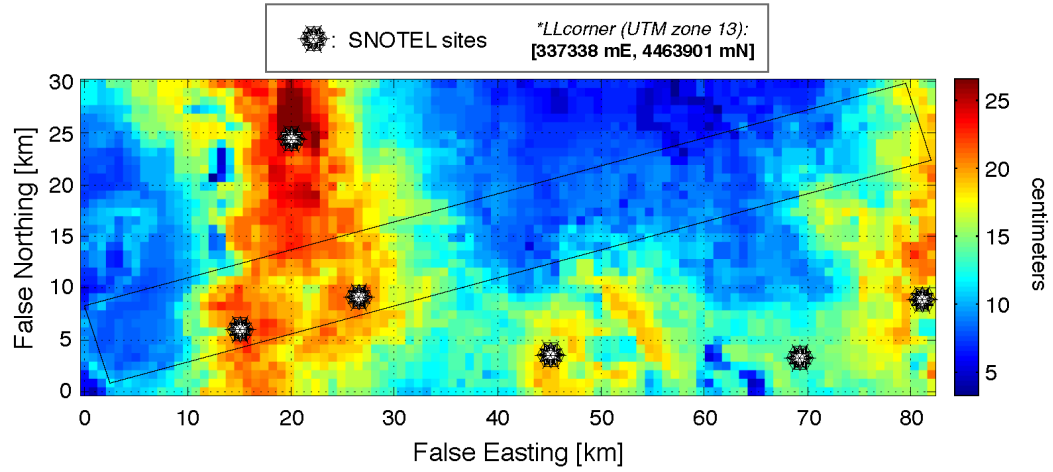


Figure 3.2: SNODAS estimates of snow water equivalent on February 22nd, 2007.

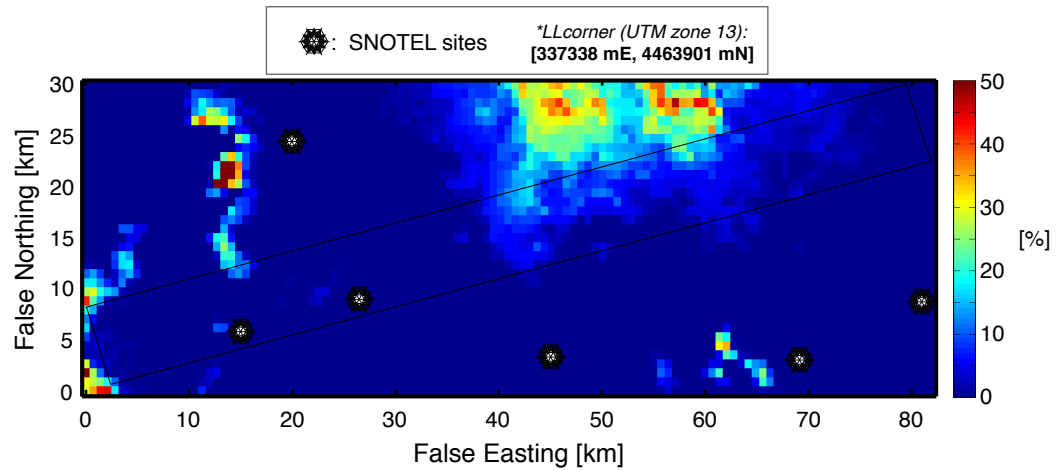


Figure 3.3: SNODAS estimates of total snow melt as a percentage of total snow precipitation from December 3rd, 2006 – February 22nd, 2007.

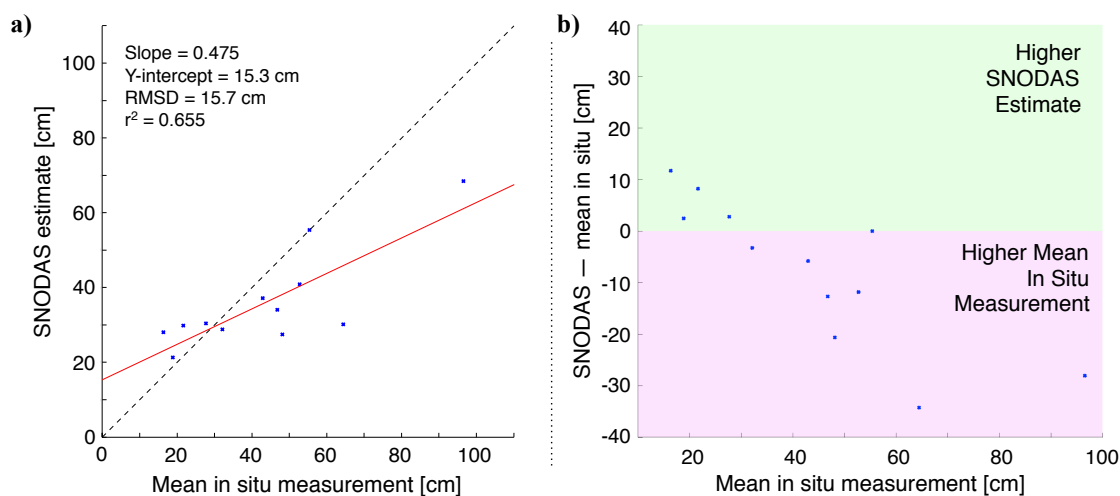


Figure 3.4: **a)** The SNODAS-estimated change in snow depth from Dec. 3rd, 2006 – Feb. 22nd, 2007 at all twelve sites from two CLPX-II Intensive Observation Periods. **b)** The difference between the SNODAS estimation and mean manual measurement as a function of measured depth at the same twelve hourglass sites.

transect site from the areal percent of coverage by nearby SNODAS pixels. This provided an area-weighted average of the SNODAS predictions centered over each in situ measurement site.

Figure 3.4a shows the relationship between the SNODAS-estimated and mean manually-measured changes in snow depth at each of the sites from the CLPX-II hourglass transects. The trend of this limited dataset appears to suggest that as the overall snow depth increases, the ability of SNODAS to estimate the amount of total snow depth change decreases. Of special note is the considerable difficulty it took to coordinate an in situ campaign as extensive as the CLPX-II manual measurements while additionally making them all within one day of the LiDAR observations. The validation dataset presented by Clow *et al.* (2012) was painstakingly gathered as well, though each site was sampled on different days throughout the winter. Most importantly, each of these coordinated efforts required thousands of field research hours

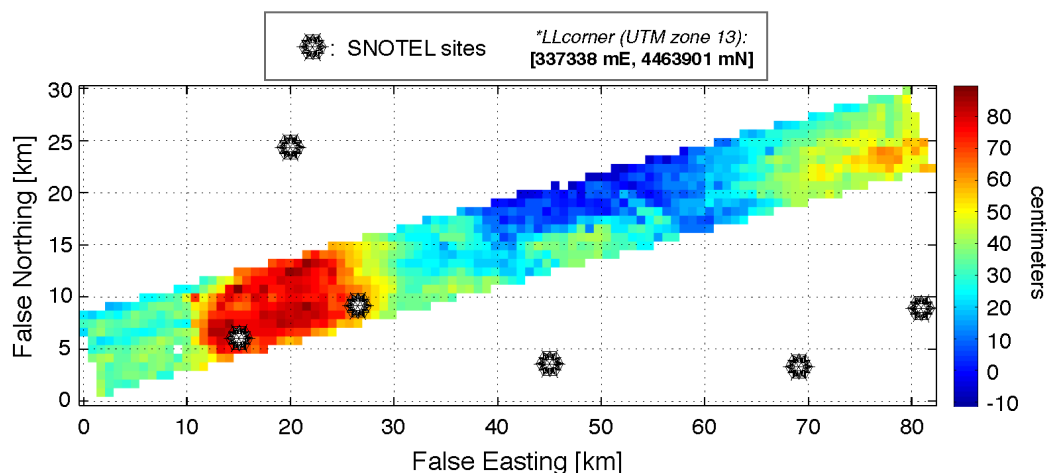


Figure 3.5: Mean LiDAR-derived 5-meter snow accumulation value [cm] within each SNODAS 30 arc-second pixel from December 3rd, 2006 – February 22nd, 2007.

to yield twelve and forty-five data points, respectively, for independent validation of SNODAS. The large extent, high resolution LiDAR observations of changes in snow depth from the CLPX-II campaign naturally provide an ideal dataset to determine where SNODAS performs well and where it has difficulty making estimates.

Interpolated to a 5-meter grid, the difference of the two bare-Earth CLPX-II LiDAR surveys provided over 100 million snow depth change values (Figure 2.2). However, since SNODAS provides estimates at a much coarser spatial scale, the high resolution values were necessarily binned into their corresponding SNODAS 30 arc-second pixels in order to compute summary statistics and make a comparison to model estimates. Additionally, the interpolated December survey vegetation and elevation surfaces were calculated at 5-meter resolution and also stored in the SNODAS pixels. The LiDAR mean snow depth change, mean elevation, and percentage of vegetation cover within each SNODAS pixel are shown in Figures 3.5, 3.6, and 3.7, respectively.

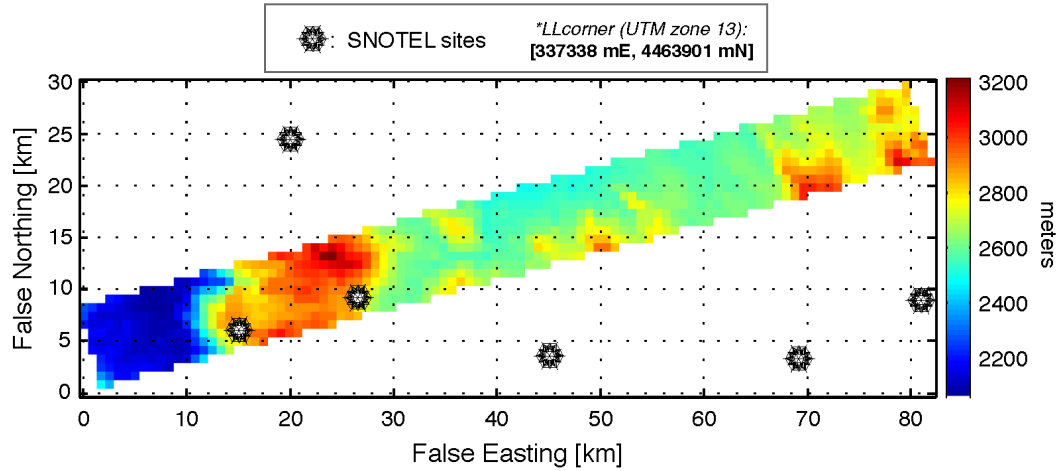


Figure 3.6: Mean LiDAR-derived 5-meter elevations [m] within each SNODAS 30 arc-second pixel.

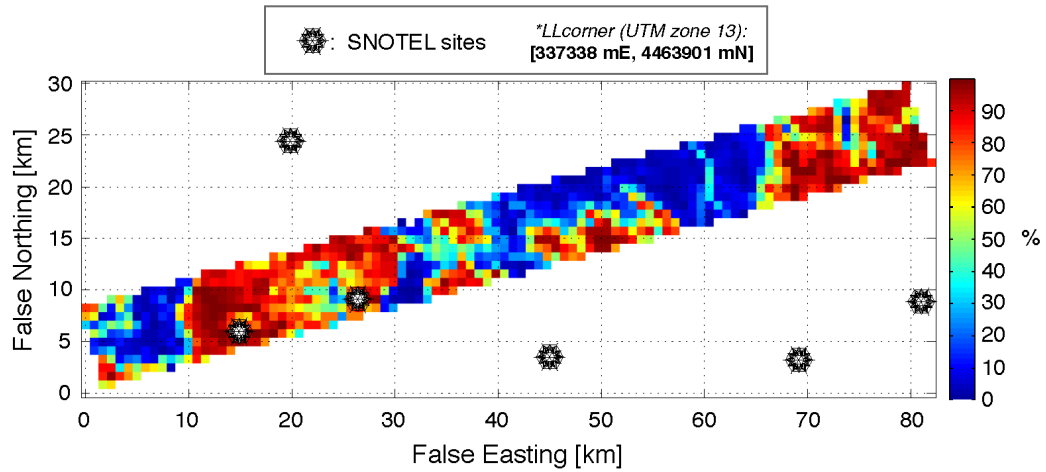


Figure 3.7: LiDAR-derived vegetation density as a percentage within each SNODAS 30 arc-second pixel.

3.2.4 Discussion

The comparison between the estimated and observed snow depth change, shown in Figure 3.8, results in an $r^2 = 0.72$, signifying a reasonably strong correlation between the model estimates and measurements. Also, since snow melt between the LiDAR flights seemed to be an insignificant portion of the snowpack evolution (Figure 3.3), the measured and estimated changes in snow depth over the study area are influenced only by accumulation, densification, and redistribution (given that this work is not considering sublimation effects).

To determine the main cause of disagreement between the SNODAS estimates and LiDAR observations of changes in snow height, seven potential physiographic parameters were culled from the LiDAR data to perform a regression analysis. The independent variables within each SNODAS pixel that were analyzed for their correlation to the model-observation discrepancies included:

1. Vegetation density [%]
2. Median vegetation height [*cm*]
3. Inter-quartile range of vegetation height [*cm*]
4. Median snow depth change [*cm*] (Dec. 3rd – Feb. 22nd)
5. Inter-quartile range of snow depth change [*cm*]
6. Median elevation [*m*]
7. Inter-quartile range of elevation [*m*]

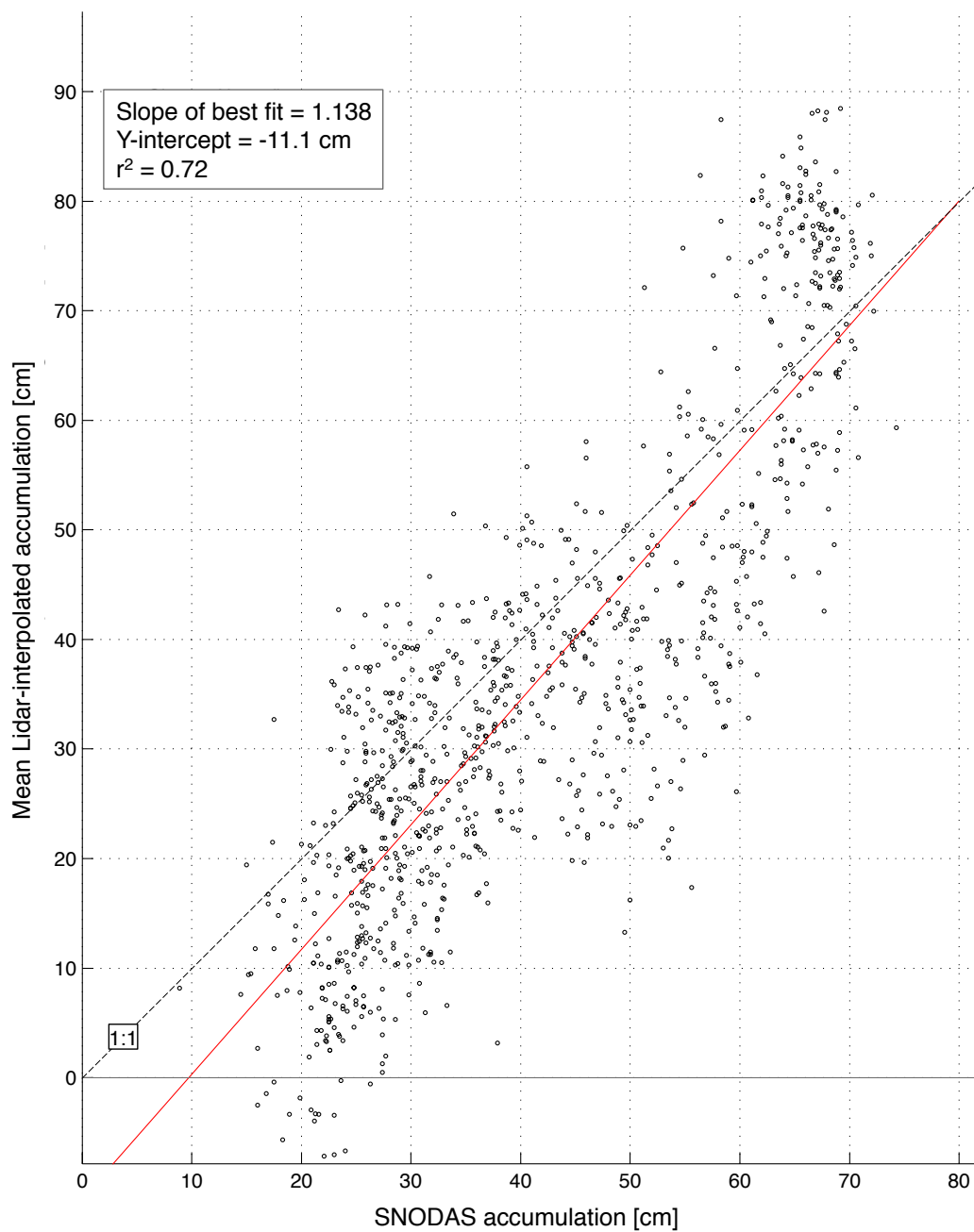


Figure 3.8: SNODAS depth change plotted against median LiDAR depth change within each 30 arc-second SNODAS pixel

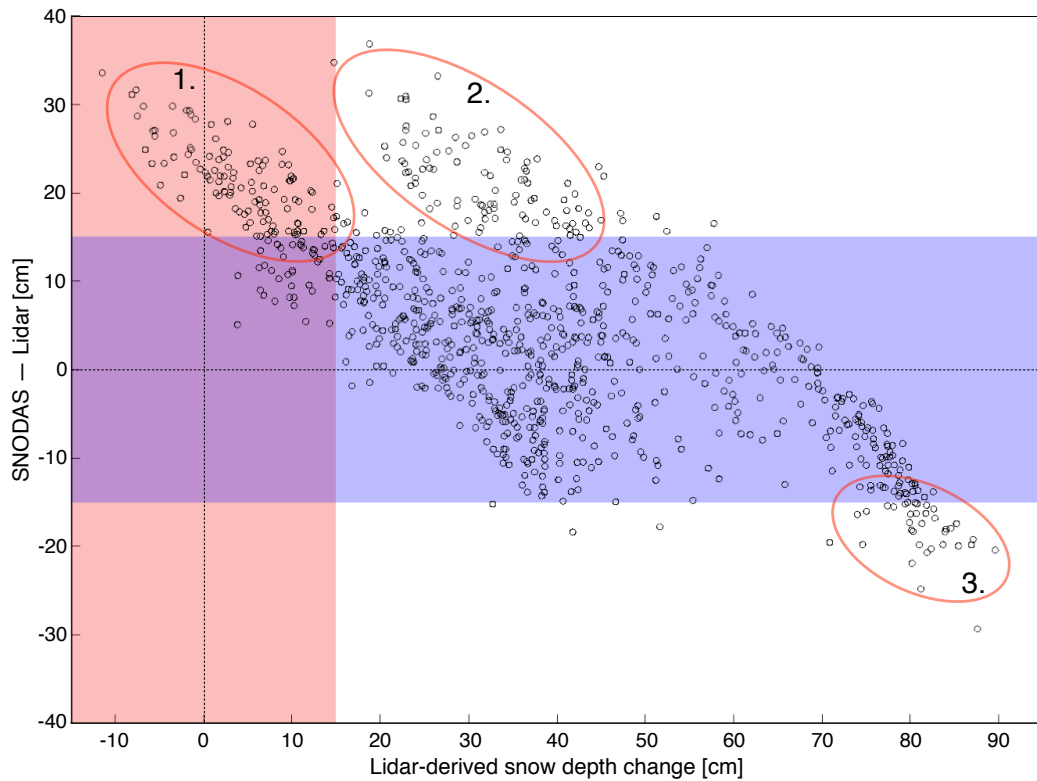


Figure 3.9: Pixel by pixel SNODAS-LiDAR differences of snow depth change plotted against the mean LiDAR depth change within each SNODAS pixel. Three distinct regions are circled that fall outside the uncertainty of the LiDAR observations, signifying a particular physiographic forcing factor present in the three specific areas.

The variable that was found to best correspond to the differences in the two datasets was the median LiDAR depth change. Figure 3.9 is a plot of the SNODAS-LiDAR difference as a function of the LiDAR change in snow depth. Three regions have been highlighted in the figure, each corresponding to portions of the difference dataset that were found to be outside the uncertainty levels of the LiDAR-derived changes in snow depth found in Chapter 2.

Each of the circled regions represent distinct geographic areas where specific factors cause relatively higher discrepancies between the modeled and remotely-sensed

changes in snow depth. The blue horizontal stripe in the figure represents the ± 15 cm that the uncertainty in LiDAR can reasonably account for in the SNODAS-LiDAR comparison.

Region #1 is comprised of pixels that SNODAS estimated to have a larger positive change in snow depth between LiDAR acquisitions. However, the LiDAR snow depth changes within these pixels are well below the trusted LiDAR uncertainty level (the pink vertical stripe). These pixels are located in the North Park region of the survey area, where the flat landscape is densely populated by low sagebrush (\approx less than 30 cm) and high winds frequently scour the snow above and near the height of the sage throughout the winter (HP Marshall, personal communication). The snow that remains is therefore packed between the low vegetation and the snow height changes very little throughout the year once it has reached a height similar to the sagebrush. SNODAS does incorporate a sublimation factor due to wind into the accumulation model, but the SNOTEL stations that are used in the assimilation step are located a good distance from the North Park area, and so wind speeds and directions are not well-represented in the area. The locations of the region #1 pixels are roughly delineated in Figure 3.10.

Pixels that comprise region #2 in Figure 3.9 are where snow depths are similarly estimated by SNODAS to have changed more than observed by the LiDAR. However, the geographic location of the pixels are in a region with higher snow accumulation totals, which are above the lower LiDAR uncertainty level of 15 cm. Again delineated in Figure 3.10, these pixels are nestled directly to the east of Rabbit Ears Pass where the Columbine SNOTEL station provides assimilation data for SNODAS. Since the relative error of the LiDAR observations is small and a large gradient can be seen

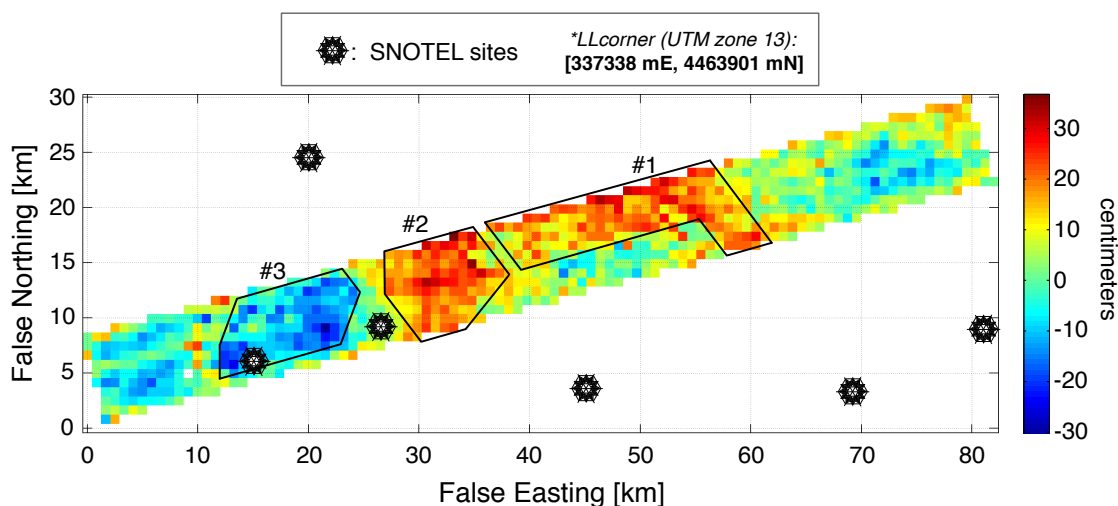


Figure 3.10: Pixel by pixel SNODAS-LiDAR differences of changes in snow depths. Hot colors are where SNODAS estimated a larger change in snow depth, while cold colors show where LiDAR observed a larger change.

in the LiDAR changes in snow depth (Figure 3.5), this discrepancy can likely be attributed to SNODAS over-distributing the SNOTEL information to areas of lower elevations and vegetation types.

Finally, the region #3 pixels represent an area where the upscaled LiDAR changes in snow depth are significantly larger than the SNODAS estimates. These pixels occur primarily in topographically complex areas with exceptionally high snow totals and dense coniferous forests, once again outlined in Figure 3.10. The probable controlling factor of underestimation by SNODAS in this region is the sub-kilometer scale heterogeneity of snow distribution caused by both vegetation and topography. SNODAS has been found to underestimate snow depths in similar forested alpine terrain (Anderson, 2011), so this result is not unexpected. The next section delves further into the issue of hillslope- and micro-scale variability by applying a wind redistribution model to a portion of the survey area.

Of special note is that NASA's Airborne Snow Observatory (ASO) mission will be collecting weekly high resolution LiDAR snow depth data for the 2012-13 – 2015-16 winter seasons over the Tuolumne Basin in California's Sierra Nevada Mountains as well as large regions of the Rocky Mountains in Colorado and Wyoming. These large-scale datasets will be able to provide additional validation for SNODAS, to say nothing of the other myriad hydrological questions that will be addressed by the campaign.

3.3 High-Resolution Wind Redistribution

Modeling

3.3.1 Introduction

In seasonal snowpacks, many factors actually affect the spatial variability of snow depth at the hillslope scale, including short- and long-wave radiation, vegetation density, and topography. But it has previously been shown that the largest cause of snow depth variability in treeless environments is wind during storm events (Elder *et al.*, 1991; Seyfried and Wilcox, 1995; Luce *et al.*, 1998). Strong winds transport loose snow from windward to leeward slopes, preferentially depositing much of the airborne grains into drifts.

The findings presented in Clow *et al.* (2012) reveal a large dependence on wind transport processes of snow for accurate prediction of SWE by SNODAS. Therefore, the second section of this chapter analyzes the wind redistribution component of the *Isnobal* energy balance snowmelt and runoff prediction model suite described in Winstral and Marks (2002) by studying a small wind-scoured portion of the CLPX-II 5-meter LiDAR DEM from the December “early season” acquisition. Previous work with this wind model has considered the wind’s effect on turbulent heat fluxes, which in turn influence sublimation and snow melt, in addition to accumulation patterns from redistribution. But due to the timing of the CLPX-II LiDAR surveys, this work only considers wind redistribution effects during the accumulation period.

Modeling how wind affects snow redistribution in heterogeneous terrain from first principles is computationally intensive and requires knowledge of the forcings at a resolution that is typically not available. Complex physics-based models have been

developed to predict where drift and scour zones develop using meteorological and topographical data (Lehning *et al.*, 2006; Liston and Sturm, 1998), but operational use of such models at scales needed for water resource planning and avalanche forecasting is not currently practical. Conversely, the wind model described in Winstral *et al.* (2009) requires merely an input DEM and calculates terrain parameters for given up-wind directions in order to predict areas of drift and scour due to wind redistribution. Meteorological information is added at a later step for incorporation into the *Isnobal* mass- and energy-balance snow model (Winstral and Marks, 2002).

Even though the complexity and computational efficiency of these models have varied significantly, the resolutions of the model input DEMs have typically been 10–30 meters. But topography and vegetation can change dramatically in complex alpine terrain in length scales much less than 10 meters. To account for this complexity, the portions of the CLPX-I and -II high resolution LiDAR DEMs are input into the wind model to observe small-scale changes in terrain, which are then compared with the LiDAR-derived snow depth data. A similar method was implemented by Schirmer and Lehning (2011), which concluded that the output parameters from the wind model are comparably significant to snow depth measurements from repeated terrestrial LiDAR scans.

Finally, of the nine ISAs surveyed during CLPX-I only the Walton Creek site was revisited during CLPX-II, thereby providing three independent measurements of the snow depth distribution at different times during the winter accumulation season at this site. These high resolution datasets, all timed before the onset of the melt season, furnish evidence of the interannual consistency of snow depth discussed in Deems *et al.* (2008) and Sturm and Wagner (2010). The observed consistency patterns of drifting

and scouring at Walton Creek are compared to the patterns obtained by the wind redistribution model terrain parameters.

3.3.2 Study Area

This study focused on a heavily wind-affected area near Rabbit Ears Pass in the southern portion of the Park Range of Northern Colorado. The area is split into two 1 km² subareas that have been separately examined as components of the CLPX-I and CLPX-II campaigns (Figure 3.11) as well as in previous studies of spatial variability (Erxleben *et al.*, 2002; Deems *et al.*, 2006; Trujillo *et al.*, 2007).

For the CLPX-I campaign, the Walton Creek Intensive Study Area (ISA) was selected to represent an environment with a very deep, wind-affected snowpack with sparse conifer groves, dense underbrush, and easy accessibility (Cline *et al.*, 2009). Airborne LiDAR surveys were performed twice for the CLPX-I mission; once on September 19th, 2003 to supply the snow-free surface and again on April 9th, 2003, the approximate date of maximum snow water equivalent.

Located just a few hundred meters to the east of the Walton Creek ISA lies the Dumont Lake study area, which was intensively sampled for snow depth during the CLPX-II campaign in conjunction with the two LiDAR surveys of December 3rd, 2006 and February 22nd, 2007. These manual measurements helped constrain remote sensing uncertainty for the LiDAR surveys but also revealed the difficulty for in situ measurements to effectively sample snow depths in complex terrain like that of the Rabbit Ears Pass area. This is true because manual measurement transects will never be able to sample at a spatial resolution similar to that of LiDAR, and at a resolution required to resolve snow drift features in this environment over a reasonable extent.

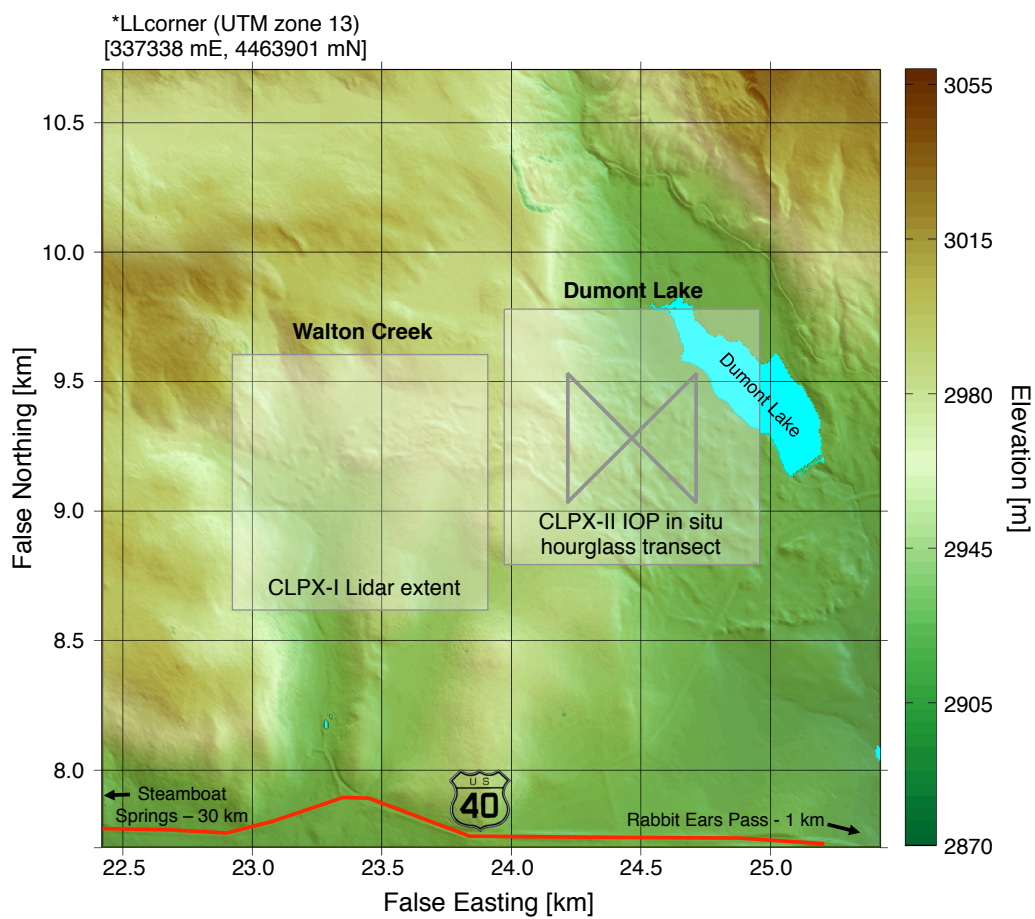


Figure 3.11: Locations of wind redistribution model study areas just north of U.S. Highway 40 in Northern Colorado. The entire area was surveyed by the CLPX-II LiDAR, but during CLPX-I only the Walton Creek site received LiDAR acquisitions. Also during CLPX-II the Dumont Lake site was the subject of an intensive ground measurement campaign.

Due to their proximity, both the Dumont Lake and Walton Creek study areas portray similar physiographic features of terrain, slope, and vegetation density. But because the Walton Creek LiDAR dataset incorporates three high resolution images of snow depth at different times and in different years, we can test the correlations between the three acquisitions to predict areas of drift and scour within the study area. After applying the wind model to derive terrain parameters within the Walton Creek site, we will execute the wind model at the Dumont Lake site to predict drifting and scouring given only a snow-free DEM.

3.3.3 The Wind Redistribution Model

The wind redistribution model described by Winstral *et al.* (2013) uses a simple slope-finding algorithm to determine the maximum upwind slope, S_x , over a user-defined search vector, d_{max} . This directional search calculation is performed beginning from each grid cell of a DEM in every upwind direction provided to the model, warranting a buffer zone surrounding the study area.

$$S_{x,d_{max}} = \max \left(\tan^{-1} \left\{ \frac{\text{vertical distance}}{\text{horizontal distance}} \right\} \right) \quad (3.1)$$

The maximum upwind slope value calculated from Equation 3.1 is then assigned to a corresponding cell position in a newly defined grid, S_x . This parameter describes the relative exposure of that cell for a given upwind direction.

Next, the model calculates the difference, S_b , between a newly calculated parameter, $S_{x,Local}$ (defined by a shorter search vector, $sepdist$) and $S_{x,Outlying}$ (again constrained by d_{max} but now beginning from the last pixel of the $sepdist$ vector). This parameter determines if any topographical features exist upwind that may sep-

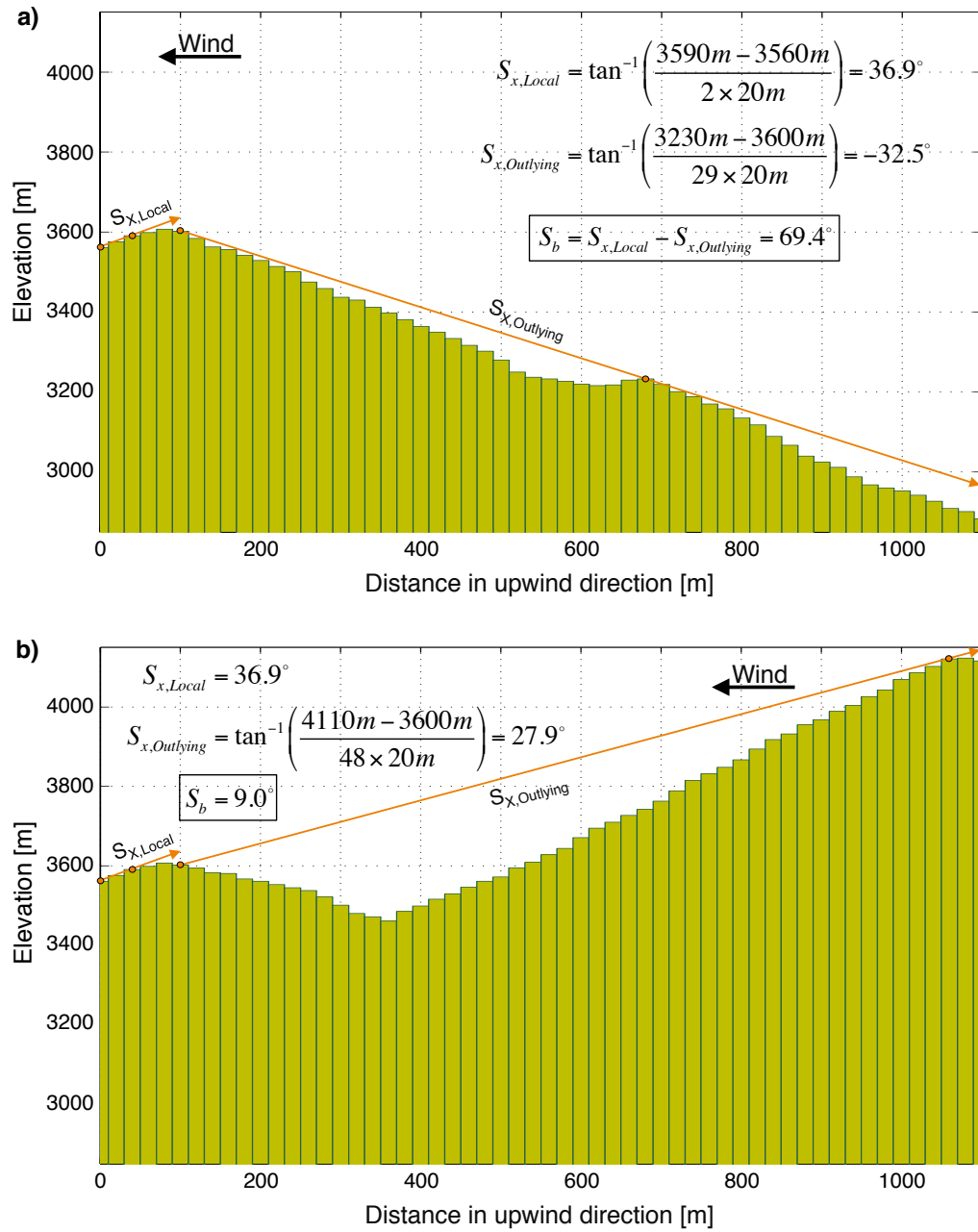


Figure 3.12: Two sample wind DEM profiles. **a)** shows a case with a high terrain break (S_b) angle, while **b)** has a much lower terrain break value.

arate wind flow, and thus allow drift formation over the cell of interest. A sample calculation is depicted in Figure 3.12 using $d_{max} = 1000m$, $sepdist = 100m$, and a hypothetical 20-meter resolution DEM.

Then, the parameters are averaged for each upwind direction in 5° increments over an encompassing 30° window to account for changes in wind direction due to small terrain features. The window-averaged terrain-break, S_b , and maximum upwind slope, S_x , parameters are calculated over each grid cell of a DEM and stored in a new gridded raster library for all user-defined upwind directions.

3.3.4 Results

The Walton Creek December LiDAR-derived 5-meter DEM was used as input for the redistribution model to produce maximum upwind slope and terrain break parameters. The prevailing winds for the site are very predominantly out of the West, as shown in Figure 3.13, so the terrain parameters derived for the 270° upwind direction were used for comparison with LiDAR-derived snow depths.

The image of the calculated $270^\circ S_b$ parameter for the Walton Creek ISA is depicted in Figure 3.15, while the LiDAR-derived change in snow depth from December to February is shown in Figure 3.16. The circled drift areas in the images signal qualifiable trends between the two datasets. Certain portions of the terrain-modeled image reveal large values of S_b that do not represent areas of drift formation (e.g., the northwest and southwest corners), but these may be explained by other factors such as incoming solar radiation and upstream vegetation that blocks the wind, calling for further investigation.

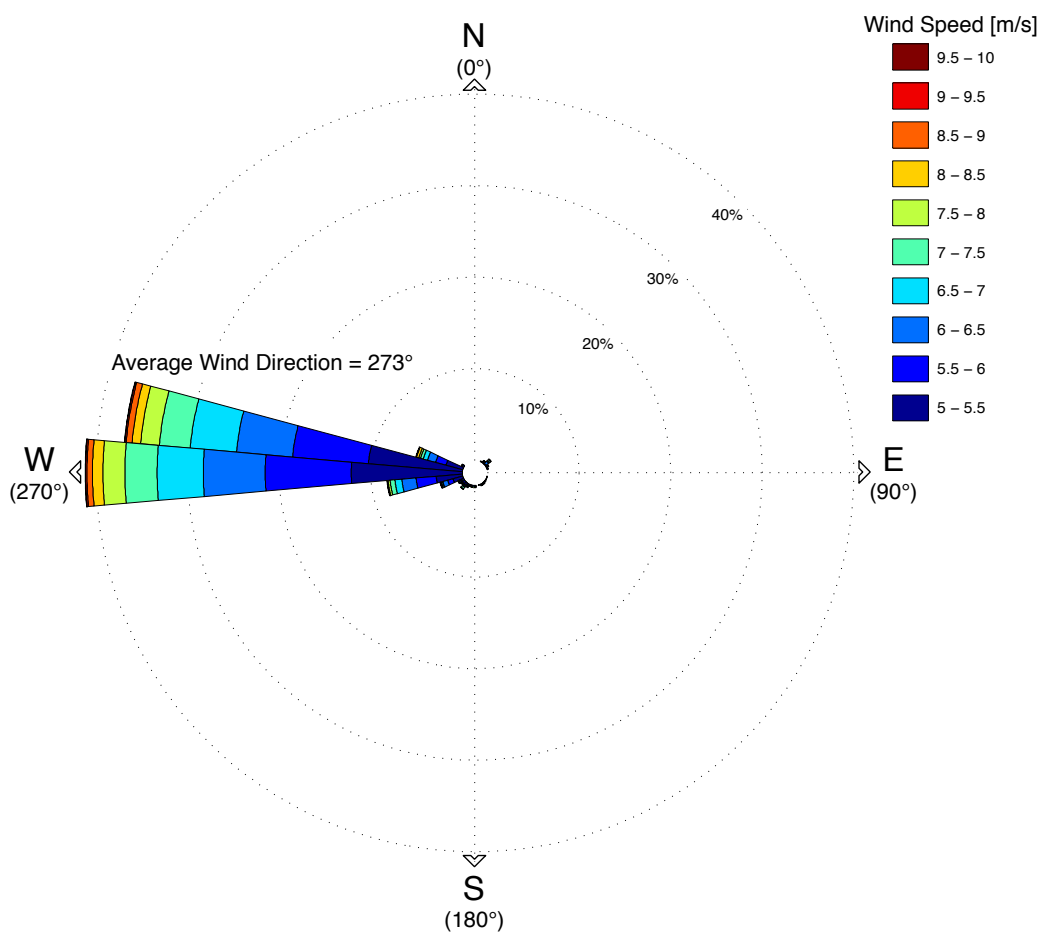


Figure 3.13: Wind rose of Walton Creek meteorological station from September 2002 – May 2003. Only depicted are measurements of wind speeds capable of lifting and redistributing snow (Li and Pomeroy, 1997). An overwhelming majority of these high winds came from the due west direction.

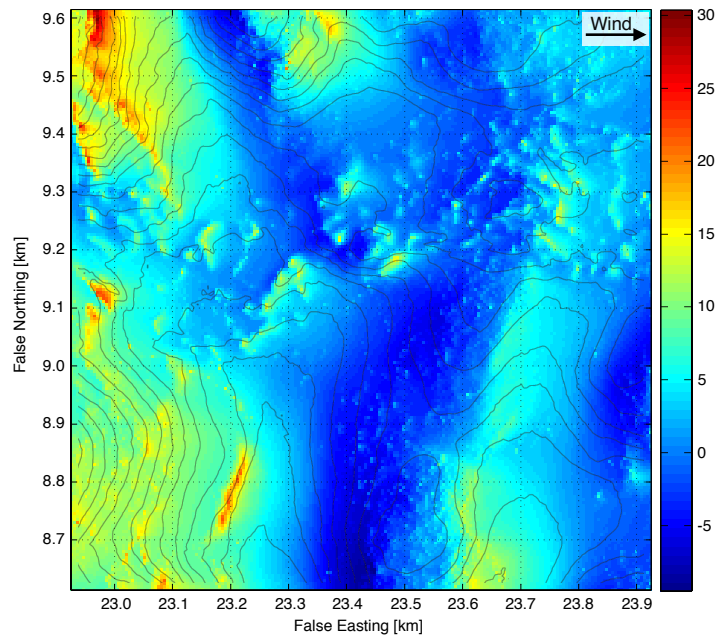


Figure 3.14: Walton Creek maximum upwind slope parameter, S_x (in degrees), from 5-meter DEM using the 270° upwind direction and $d_{max} = 150m$.

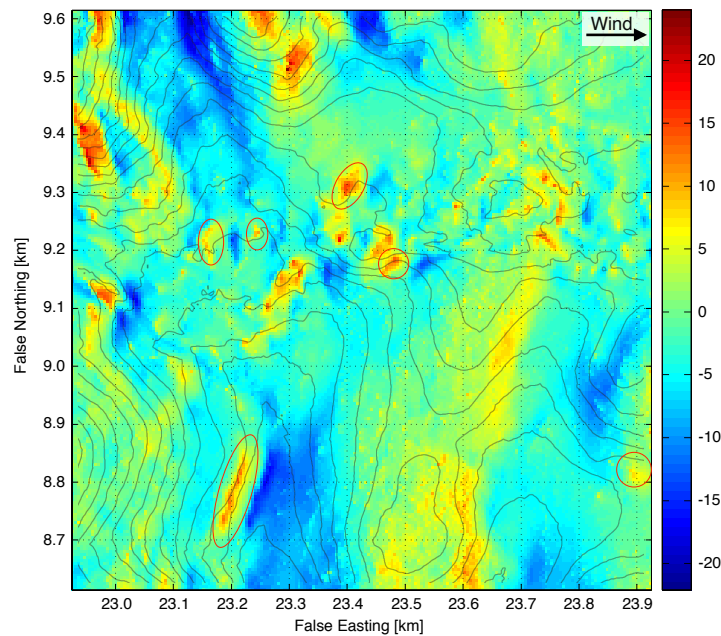


Figure 3.15: Walton Creek terrain-break parameter, S_b (in degrees), from 5-meter DEM using 270° upwind direction, local $d_{max} = 50m$ and outlying $d_{max} = 150m$.

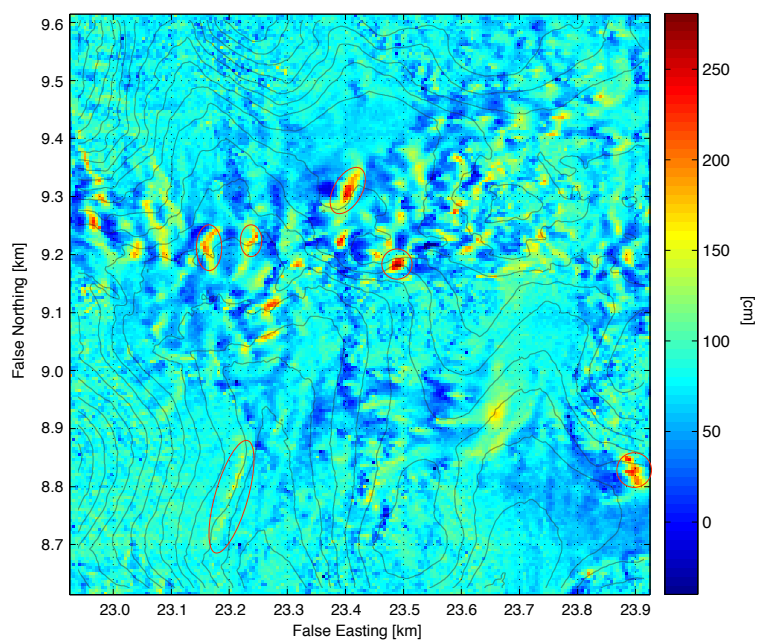


Figure 3.16: LiDAR-derived, 5-meter resolution snow accumulation between December 3rd, 2006 and February 22nd, 2007.

Interannual Consistency

LiDAR acquisitions are the only method currently available to observe snow accumulation at such a high spatial resolution and extent. Manual sampling transects are helpful for estimating average snow depth and SWE in areas with similar topography, but cannot realistically sample at the same point density as a LiDAR survey. However, the major downside of acquiring LiDAR-derived snow accumulations is the high cost and difficulty of gathering accurate data. Though costs for LiDAR surveys are quickly falling, to only have a need to survey a particular location two times (the snow-free and snow-covered surface) for predicting the relative year-to-year snow distribution would be a great advantage for snow researchers, water managers, and avalanche practitioners.

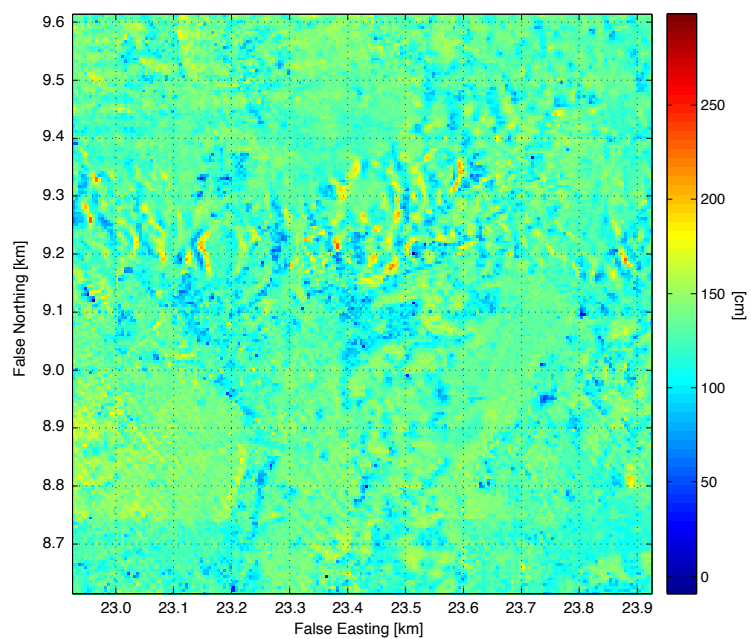


Figure 3.17: LiDAR-derived, 5-meter resolution snow depths at Walton Creek as of December 3rd, 2006.

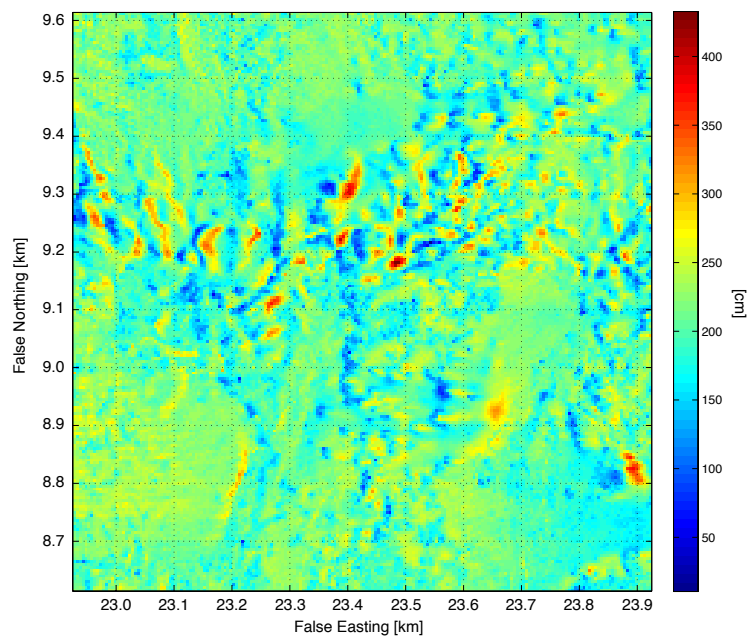


Figure 3.18: Snow depths at Walton Creek as of February 22nd, 2007.

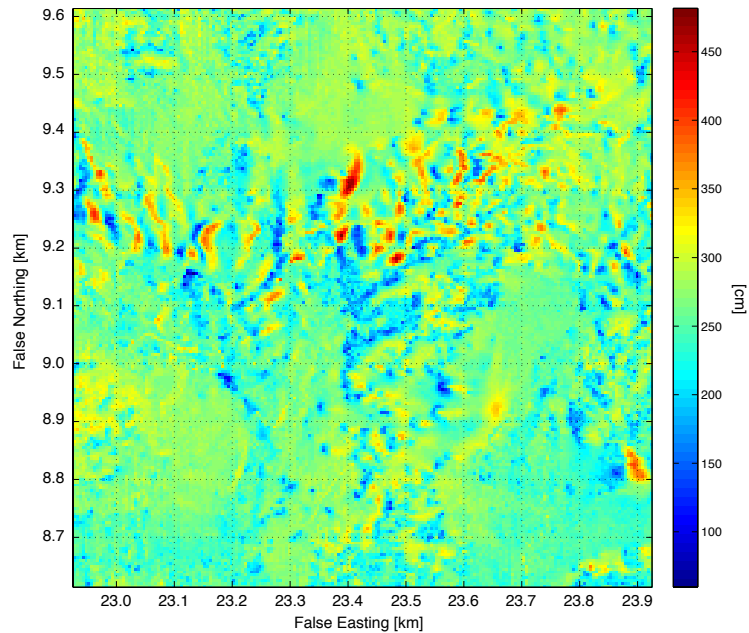


Figure 3.19: Snow depths at Walton Creek as of April 9th, 2003.

Fortunately, four LiDAR flights were flown in different years over the Walton Creek ISA as a component of the CLPX-I and CLPX-II campaigns, resulting in three separate observations of the snow distribution at distinct moments of the accumulation season. Designated as the December, February, and April surveys (Figures 3.17–3.19), the distributions have been rigorously compared to one another to detect any quantifiable correlations between the observations.

First, snow depths were standardized by subtracting the mean and dividing by the standard deviation of the depth distribution for each survey. Next, three sets of correlations were obtained by multiplying the standardized depths for December to February, December to April, and February to April, respectively. Finally, the cube-root of the product of the three correlation sets resulted in a final metric for interannual consistency of snow distribution (Figure 3.20). This method worked to

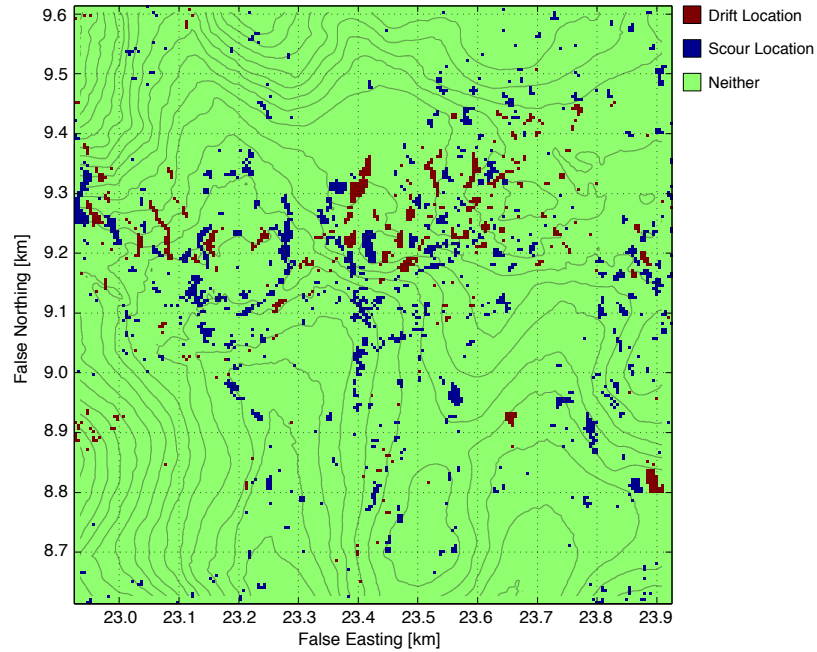


Figure 3.20: Statistically-determined drift and scour locations at the Walton Creek study area from three separate winter LiDAR acquisitions.

expose all snow depth pixels that were persistently much higher or much lower than the overall mean snow depth for the study area (Figure 3.21). The fact that the method located many of the drifting and scouring grid cells indicates an existing interannual trend for the snow depth distribution at Walton Creek.

Distribution Consistency and Wind Modeled Terrain Parameters

The drifting and scouring locations developed in the previous section using multi-temporal LiDAR datasets can also be used to determine the effectiveness of the S_b and S_x terrain parameters for predicting drift and scour locations in similar terrain. It must be mentioned, however, that the interplay between vegetation and spatial variability at Walton Creek is not investigated in this work because only the

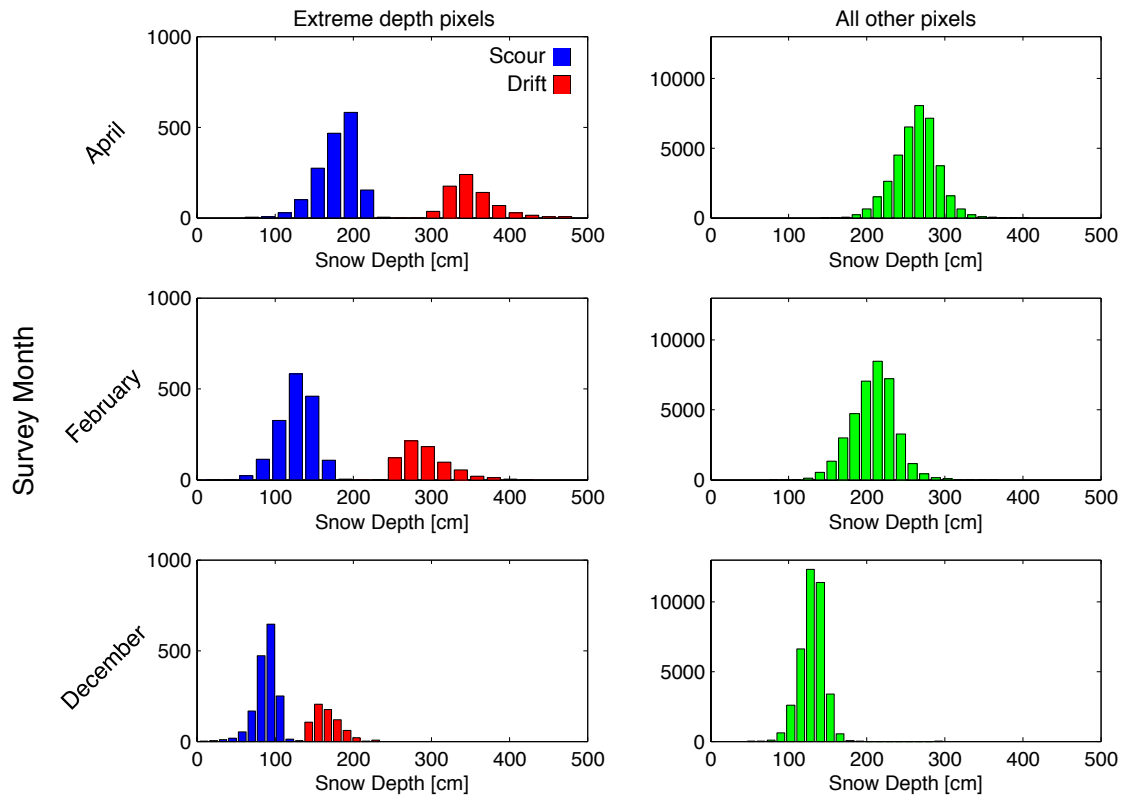


Figure 3.21: Histograms of snow depth after applied classification scheme for each ‘Snow-On’ LiDAR survey. Classification separates the persistently drifted and scoured pixels (extreme values) from other values that remain nearer to the mean of each survey.

vegetation-filtered DEM has so far been applied to the wind model. Future work will look into the proportional amount of vegetation and terrain effects on wind-blown snowpacks.

The pixels representing neither consistent scouring nor drifting in Figure 3.20 were removed from both the modeled S_x and S_b parameters. The distributions of S_x and S_b were then plotted in Figure 3.22, where the point of intersection between the drift and scour cell peaks can be considered the optimal cutoff values for S_b and S_x for predicting drifting and scouring in similar environments. For all cells, if $S_b \geq -0.4^\circ$ and $S_x \geq 3.4^\circ$, then that particular cell has the possibility of drift formation. Similarly, if $S_x < 3.4^\circ$, then that cell is likely a scoured location.

Because of their close proximity, the Dumont Lake study area was used to test the applicability of the optimal terrain parameter cutoff values determined at Walton Creek. Shown in Figure 3.23, the LiDAR-observed snow depth change distribution at Dumont Lake exhibits similar patterns to the Walton Creek site. The parameter cutoff values of $S_x = 3.4^\circ$ and $S_b = -0.4^\circ$ were used to trim predicted drift (Figure 3.24) and scour (Figure 3.25) locations from the true observed snow distribution.

The results qualitatively show that when the correct wind redistribution model cutoff values are known for a particular area, the terrain parameters can effectively determine high and low snow accumulation cells. The areal extent could easily be increased while remaining at a high 5-meter resolution in order to determine fine-scale spatial variability over very large regions, given that the landscapes for the determined parameter cutoff values remain somewhat similar.

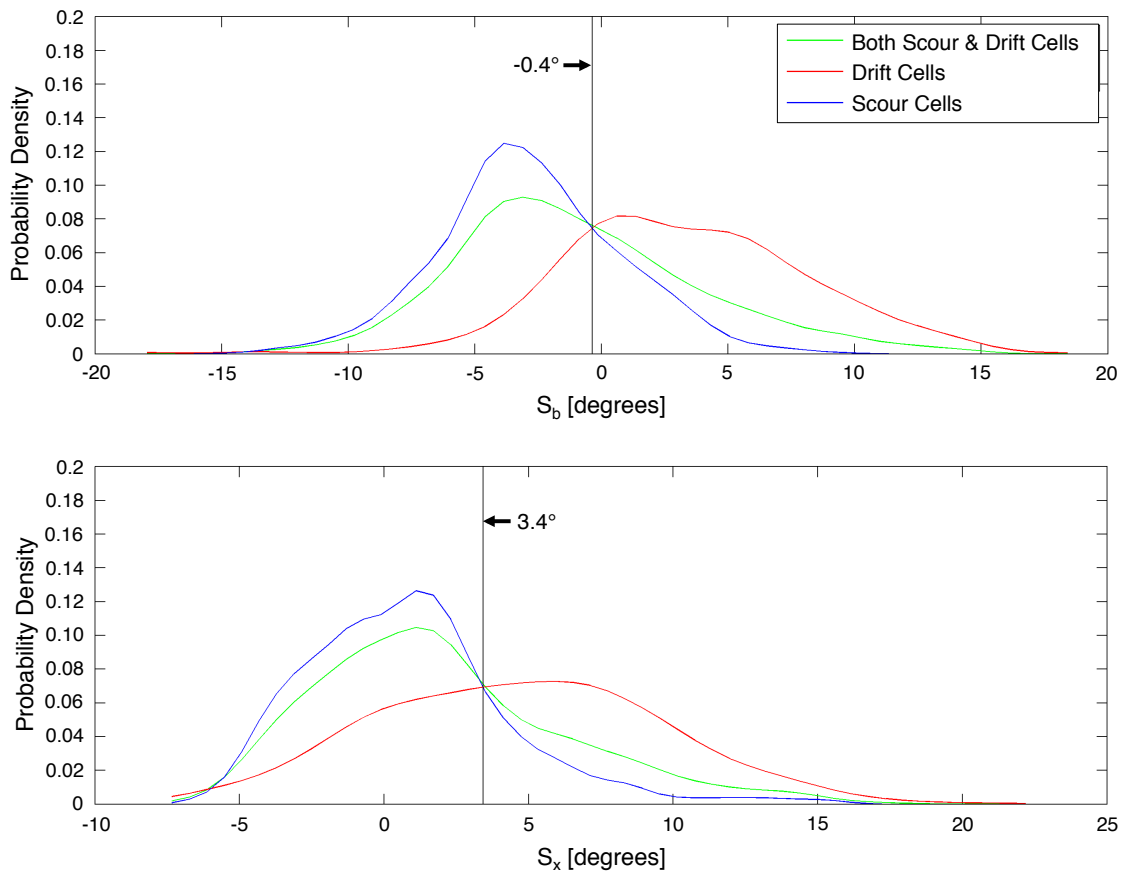


Figure 3.22: Probability density functions of S_b and S_x at Walton Creek for known drift and scour cells from interannual consistency study.

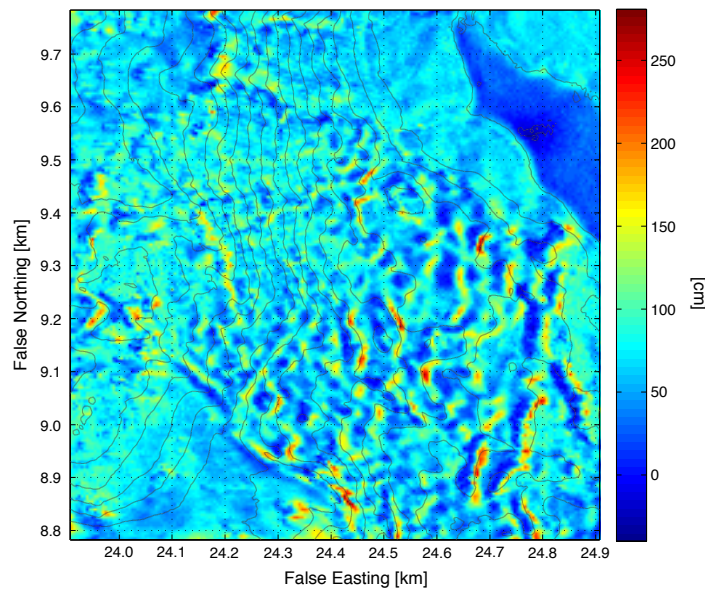


Figure 3.23: LiDAR-observed changes in snow depth at Dumont Lake study area for December 3rd, 2006 – February 22nd, 2007. The lake can be seen in the northeastern corner.

3.3.5 Discussion

Micro-scale terrain features significantly affect the spatial distribution of snow in seasonal snowpacks. Using high resolution, LiDAR-derived snow-free DEMs, a wind redistribution model developed by Winstral and Marks (2002) has the potential to accurately predict where drifts will form and scouring will occur over complex terrain.

Using one snow-free and three snow-covered LiDAR surveys over a small 1km^2 study area, we were able to statistically analyze the spatial snow depth distributions to determine areas of drifting and scouring. With these locations known, the wind redistribution model was implemented to calculate the S_x and S_b terrain parameters over the site. The locations of confirmed drifts and scour cells were used to discover cutoff values of the model terrain parameters where below or above drifting and

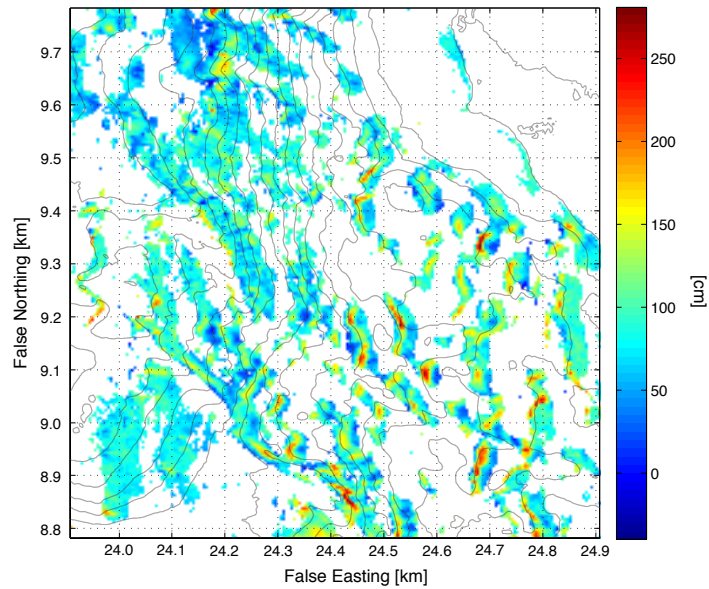


Figure 3.24: Regions from the Dumont Lake LiDAR-derived change in snow depth raster where the terrain break parameter $S_b \geq -0.4^\circ$, and the maximum upwind slope parameter $S_x > 3.4^\circ$

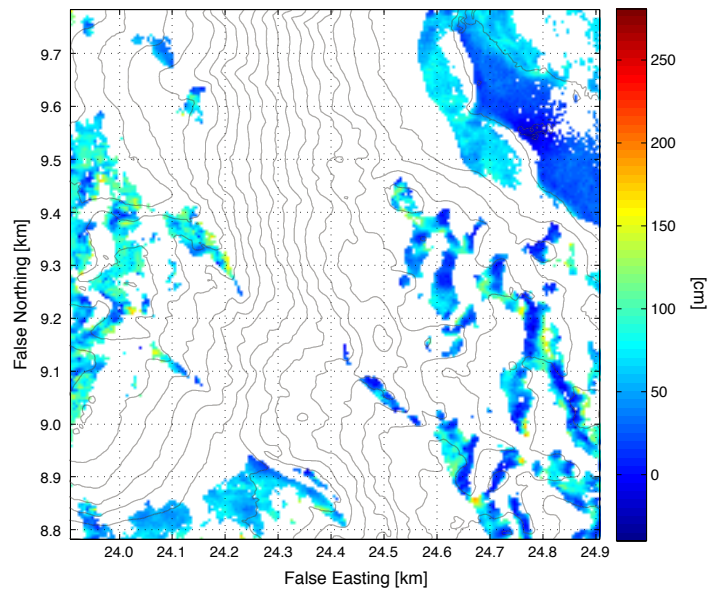


Figure 3.25: Regions from the Dumont Lake LiDAR-derived change in snow depth raster where the maximum upwind slope parameter $S_x < 3.4^\circ$

scouring was likely to occur.

Then, at a nearby site, the wind model was again executed and the terrain parameter cutoff values used to designate drift and scour cells. Because we also know the spatial snow distribution at this site from LiDAR, we were able to qualitatively check the ability of the wind model to predict drifting and scouring. The results encourage a larger study of this method in regions where LiDAR-derived distributions of snow depths are known.

CHAPTER 4:

MEASURING SNOW DEPTHS WITH TIME-LAPSE PHOTOGRAPHY

4.1 Summary

Previous chapters considered the measurement and modeling of seasonal snow's spatial variability at a single moment in time, but now we will turn to addressing the difficulty of making high resolution, spatially-distributed temporal measurements of snow depth over broad mountain regions. We introduce a lightweight, inexpensive technique to record hourly snow depths at multiple locations using time-lapse photography and image processing techniques. Preliminary results are presented that agree closely with nearby standard ultrasonic sensors and encourage a wider implementation to make point depth measurements over a wide spatial scale and at a high temporal resolution. Finally, we detail the drawbacks of using photography to measure snow depth during cold and dark winter months and outline plans to increase measurement capabilities at night and during fierce weather.

4.2 Introduction

Remote sensing measurement techniques such as LiDAR are beginning to emerge as viable methods to observe snow depths at extremely high spatial resolutions over large areas. However, the evolution of mountain snowpacks over *time* is an equally

important problem to consider. In order to ideally model seasonal snow accumulation and ablation, researchers would need information about snow depth and density at *all* times and over *all* space. While this is impossible in practice, advances in technology are slowly allowing us to answer certain questions about spatial and temporal variability of snow with more and more confidence.

To better understand hillslope-scale snow processes, researchers necessarily began by studying instantaneous glimpses of the snowpack's spatial distribution with coordinated in situ measurement campaigns (Elder *et al.*, 1991; Erxleben *et al.*, 2002) and later repeated airborne (Deems *et al.*, 2006; Trujillo *et al.*, 2007) and terrestrial (Prokop, 2008; Schirmer and Lehning, 2011) LiDAR surveys. But the complex information given by these snapshots of spatial distribution come with a very high monetary cost of instrumentation and are not yet easily automated at an hourly time-step, thus losing any ability to observe high resolution temporal snowpack evolution, which this work aims to capture.

Knowledge of meteorological conditions during accumulation events allows an approximation of the snow's grain size, density and water content; all factors that are important for snow hydrology and avalanche forecasting applications. The first systems for obtaining high temporal resolution weather data *in addition* to snow measurements were developed in the mid-1970s with the installation of the first continually monitoring SNOw TELelemetry (SNOTEL) stations in the Rocky Mountains. Maintained by the Natural Resources Conservation Service (NRCS) and still in widespread use today, these systems are able to make automated measurements for entire winter seasons, resulting in rich historical datasets used nationwide by snow hydrologists, water forecasters, and avalanche practitioners. Snow water equivalent (SWE) is mon-

itored by snow pillows, essentially large bags filled with liquid for measuring the hydrostatic pressure of the overlying snow. Additionally, most SNOTEL sites incorporate an ultrasonic sensor to automatically measure snow depth.

Nonetheless, SNOTEL information is merely a point measurement and stations are typically installed in sheltered forest glades where micro-scale weather can be relatively calm compared to the surrounding storm-scale conditions. Capturing processes that affect spatial variability of snow over extended time periods would require a network of standard ultrasonic sensors, implementation that would be difficult due to power and telemetry constraints. An alternative for observing spatial and temporal variability would be to employ time-lapse photography methods and a network of affixed snow depth markers.

Time-lapse photography has been used extensively in cold regions research to examine gradually evolving processes ranging from glacier and ice sheet retreat (Harrison *et al.*, 1992; Ahn and Box, 2010) to snow crystal metamorphism (Pinzer and Schneebeli, 2009). Post-processing for these methods can be laborious and difficult when an object is far from the camera due to slight shifts in camera position and orthorectification error. However, accurate measurements can be more easily obtained when distances to the objects of consideration are limited to the near-field.

Over the 2012/2013 winter season, two rugged, low power prototype time-lapse camera systems were deployed at easily accessible study sites to verify a new method of measuring hourly snow depths at point locations. The primary goals of this initial deployment were to test an inexpensive measurement system and to subsequently develop a pixel-counting algorithm to calculate snow depth at multiple locations for each image captured by the camera. A pair of ordinary ultrasonic depth sensors, one

located in a NRCS-maintained SNOTEL site, were used as measurement validation for the method.

Since photography can be considered a passive optical remote sensing method, there are naturally drawbacks for using it to measure snow depths: primarily an inability to capture images at night or during poor visibility conditions. Despite these limitations, the results of the method presented here were well-correlated to the ultrasonic depth measurements, presenting a new tool for researchers interested in the temporal evolution of mountain snowpacks. The main advantages of this method are the portability and low cost of the camera setup, potentially allowing several cameras to make automated depth measurements at dozens of points over entire accumulation and ablation seasons.

4.3 Methods

4.3.1 Study Sites

A prototype measurement system was installed in November 2012 at a study plot maintained by the Boise State University Center for Geophysical Investigation of the Shallow Subsurface (CGISS) within the ski area boundary of Bogus Basin Recreation Area, 16 miles northwest of Boise, ID. Located at $43^{\circ} 45' 31''$ N, $116^{\circ} 5' 24''$ W (Figure 4.1), the study plot has an elevation of 2,100 m.s.l. and is primarily south-southeast-facing with 20° – 30° slopes. Validation of the system was made possible with two nearby ultrasonic snow depth sensors manufactured by Judd Communications, LLC. The first ultrasonic sensor is located within the Bogus Basin SNOTEL site $3/4$ km to the northwest and the other just 20 meters away along a nearby ridge, maintained

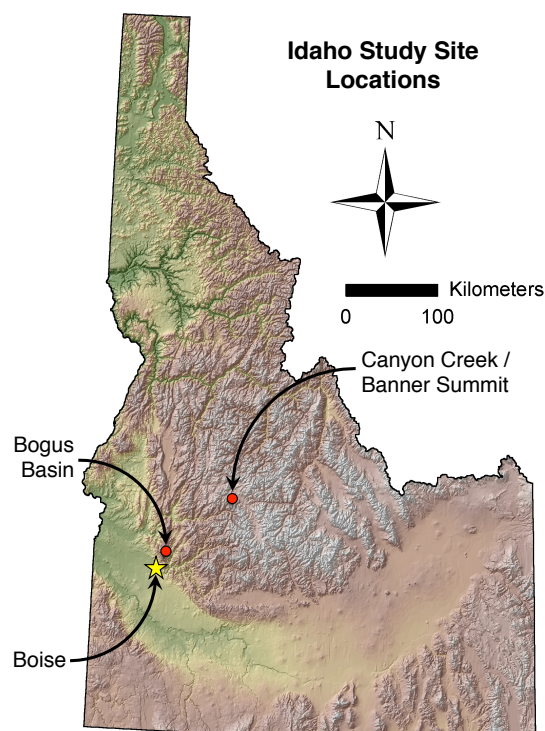


Figure 4.1: Locations of time-lapse snow depth cameras in Idaho, USA

by the Boise State University Hydrology group. As a fully functional snow study plot, the site's primary goals are to investigate snow stratigraphy evolution, spatial variability, soil moisture and resistivity, and lateral flow of melt water through the snow pack using resistivity methods, various radar systems, and an array of snowmelt lysimeters (Figure 4.2). Terrestrial LiDAR surveys of the study site were conducted on October 12th, 2012 and March 13th, 2013, respectively, using a Riegl VZ-1000 3D laser scanner to provide reference surfaces of spatial snow depth distribution.

The second camera was planned to be installed adjacent to a frequent avalanche starting zone 530 meters above State Highway 21 and three miles south of Banner Summit in the Sawtooth Mountains of Central Idaho ($44^{\circ} 14' 20''$ N, $115^{\circ} 12' 9''$ W,

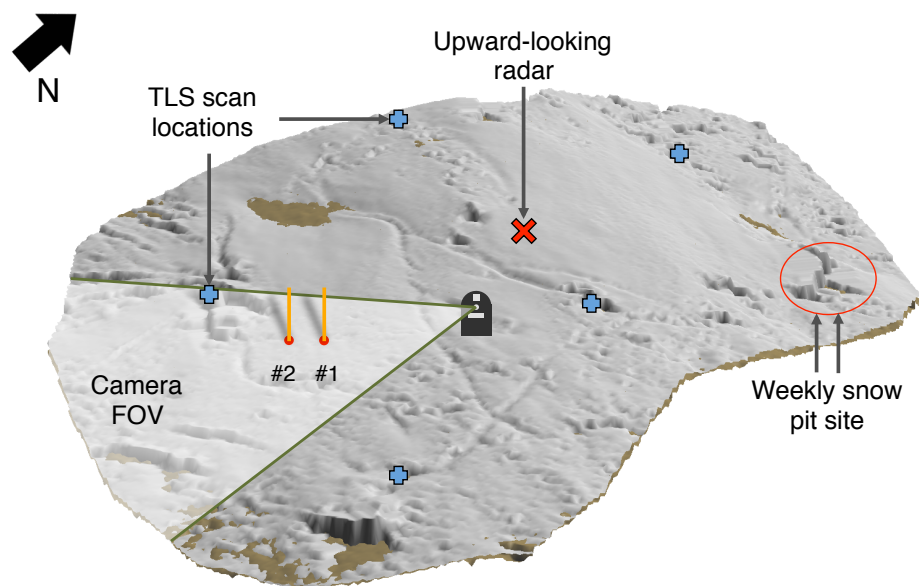


Figure 4.2: Bogus Basin study site layout showing location of the time-lapse camera with field-of-view and snow depth markers as well as snow pits and upward-looking radar. Snow-free (brown) and snow-covered (white) 20 cm digital surface models were obtained from repeated terrestrial laser scans.

Figure 4.1). A 5-meter steel depth post was to be secured with cement and guywires and depth would be monitored all winter long. However, weather conditions worsened before completion of the site installation and the decision was made to relocate the prototype across the canyon to a heavily wind-scoured ridge site that would remain more accessible throughout the winter. Though the site location has a similar elevation to the Bogus Basin study plot at 2,150 msl, the local weather is much more severe and wind speeds can routinely surpass 35 m/s during winter storms. Storms over the area also exhibit large variations in temperature and wind directions, resulting in a transitional snowpack with average snow depths of 2–3 meters and large drifts and ridge cornices.

4.3.2 Instrumentation

The most cost-effective time-lapse cameras currently on the market are manufactured for game-monitoring and birdwatching photography. Variously manufactured by Moultrie and Wingscapes, subsidiaries of EBSCO Industries, Inc., these cameras have limited features but are lightweight, easily secured to stationary objects such as trees or rocks, and most importantly have very low power consumption. Between timed startups the camera draws merely 1–2 mV and therefore only requires two 12 volt, 9 Ah batteries to capture ten images a day for at least six months. Before deployment, the pixel size as a function of distance is calculated for each camera by taking images of fixed 10cm and 50cm orange strips from measured ranges of 10–100 meters away. Factors such as ambient air temperature and relative humidity may have a small distortion effect on the correlation, but are not considered at this time.

After all the connections have been sealed and epoxied with the batteries fixed within a waterproof electrical junction box, a complete camera system weighs in at less than fifteen pounds, allowing for distribution in remote mountain areas. Captured images are output to a high-capacity SD card that does not need to be replaced for the season duration. Finally, a bright orange depth marker is secured in the nearby soil and the distance is measured from the camera to the top, dT , and base, dG , of the marker to determine the viewing angle to limit error from pixel size distortion (Figure 4.3). At the Bogus Basin site, two depth markers were anchored into the soil to test the system's ability to make measurements at multiple points simultaneously within one image (Figure 4.4).

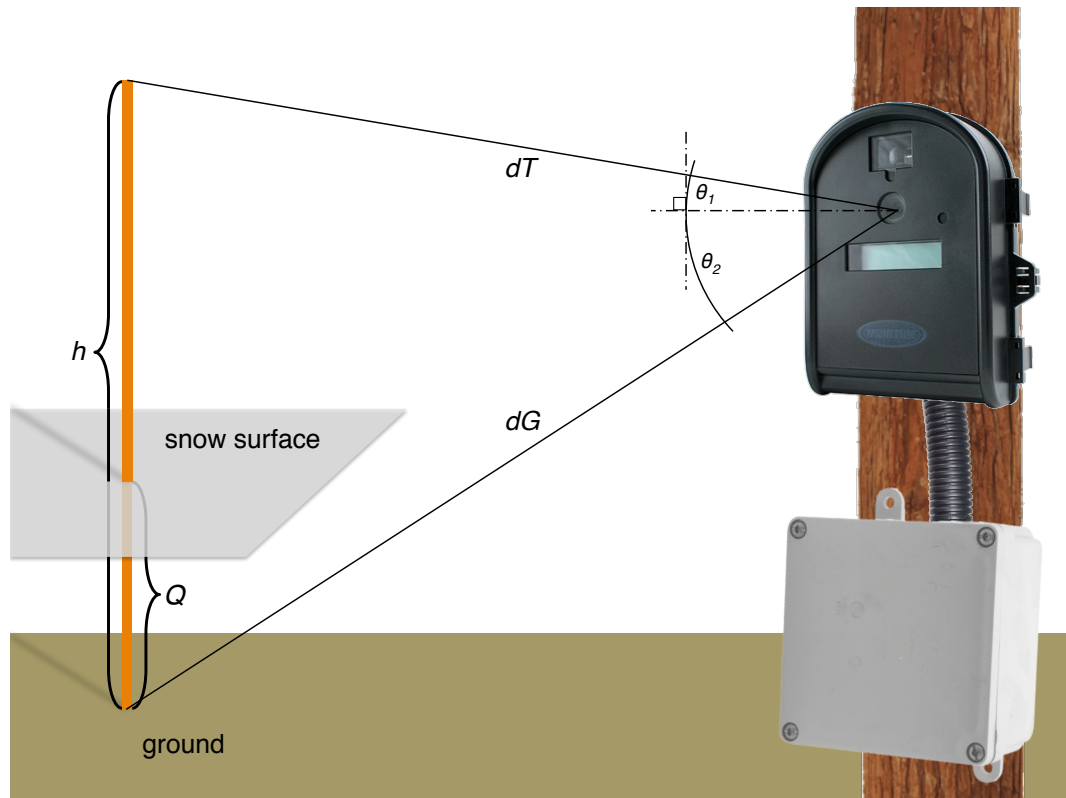


Figure 4.3: Typical time-lapse snow depth camera system arrangement. dT , dG and h are measured and pixel size as a function of distance is predetermined, permitting the calculation of snow depth, Q , for every hourly image.

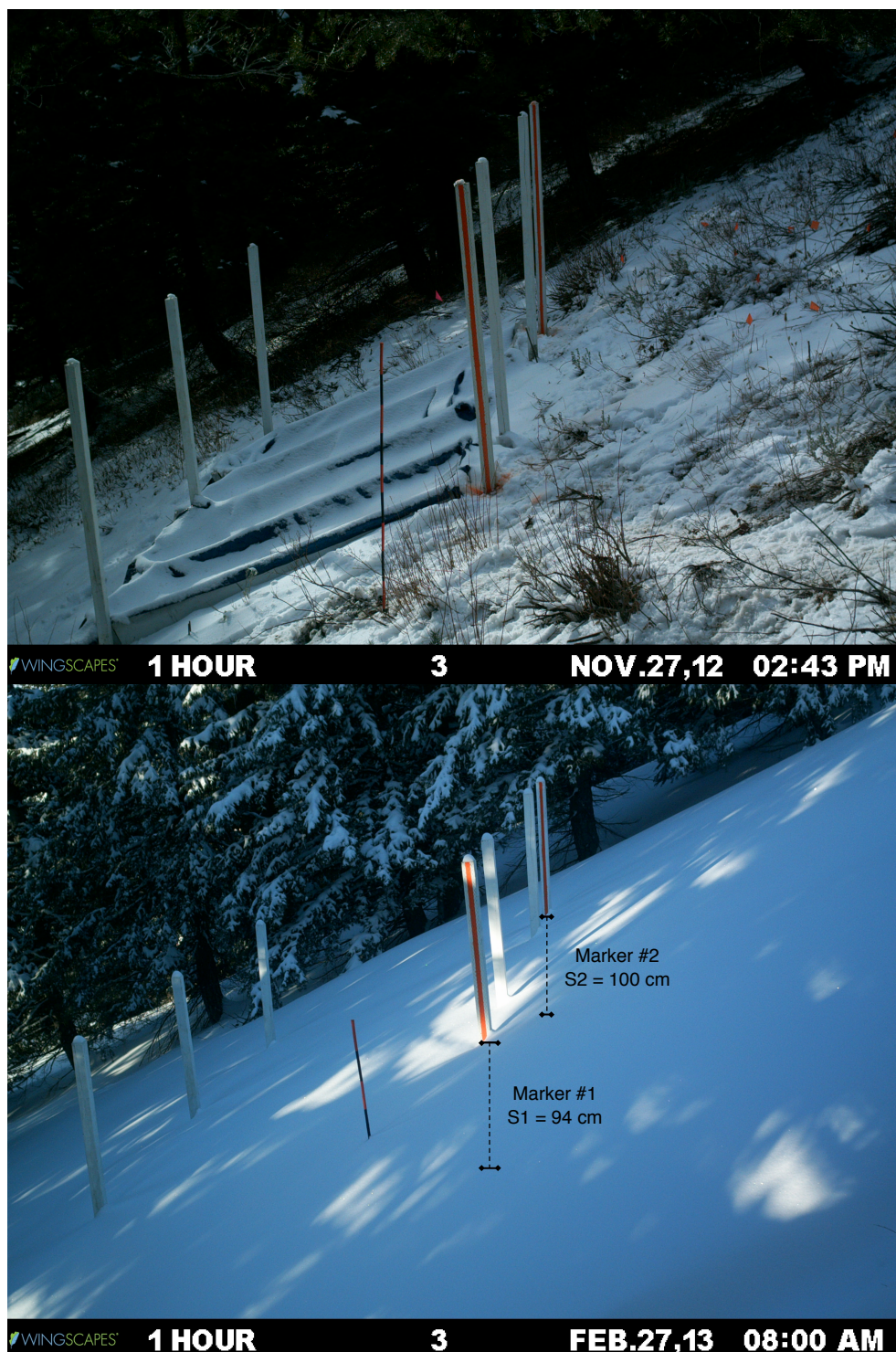


Figure 4.4: Sample images captured by the Bogus Basin study site camera with calculated snow depths displayed for both markers. Upper image was taken the day of installation.

4.3.3 Algorithm

Each camera was programmed to wake from sleep every daylight hour to capture a single image. Because the camera and depth markers were in fixed locations, it was possible to automatically track the snow surface if a large gradient existed between the pixel intensity of the white snow and an orange depth maker. The distance from the camera lens to the top and bottom of each marker was measured before the accumulation season began, to provide an estimate of horizontal error due to snow creep upon the marker and subtle camera shifts. Finally, a pixel counting process was developed to track the snow surface throughout the season.

Essentially, the algorithm clips each image to small rectangle around the last-known vertical pixel location of the marker base (Figure 4.5a), then separates and smooths the blue channel of the RGB image for ultimate consideration (Figure 4.5b). This is done because snow's spectral albedo causes the most light to be reflected in the near ultraviolet and blue visible spectrum (Wiscombe and Warren, 1980), resulting in a large intensity gradient between depth marker and snow surface. Next, row-wise minimums are calculated to create a column vector (Figure 4.5c) and the difference between subsequent elements are found (Figure 4.5d).

Because the first step of the algorithm is to clip each image to the base of the depth marker, eliminating all other portions of the image where high intensity gradients exist, the greatest change between the blue channel row minimums can be classified as the snow surface pixel row. After this row is determined, the depth conversion is performed by subtracting the pixel row of the snow-free marker base and dividing by the number of pixels per centimeter for the depth marker's predetermined distance from the camera.

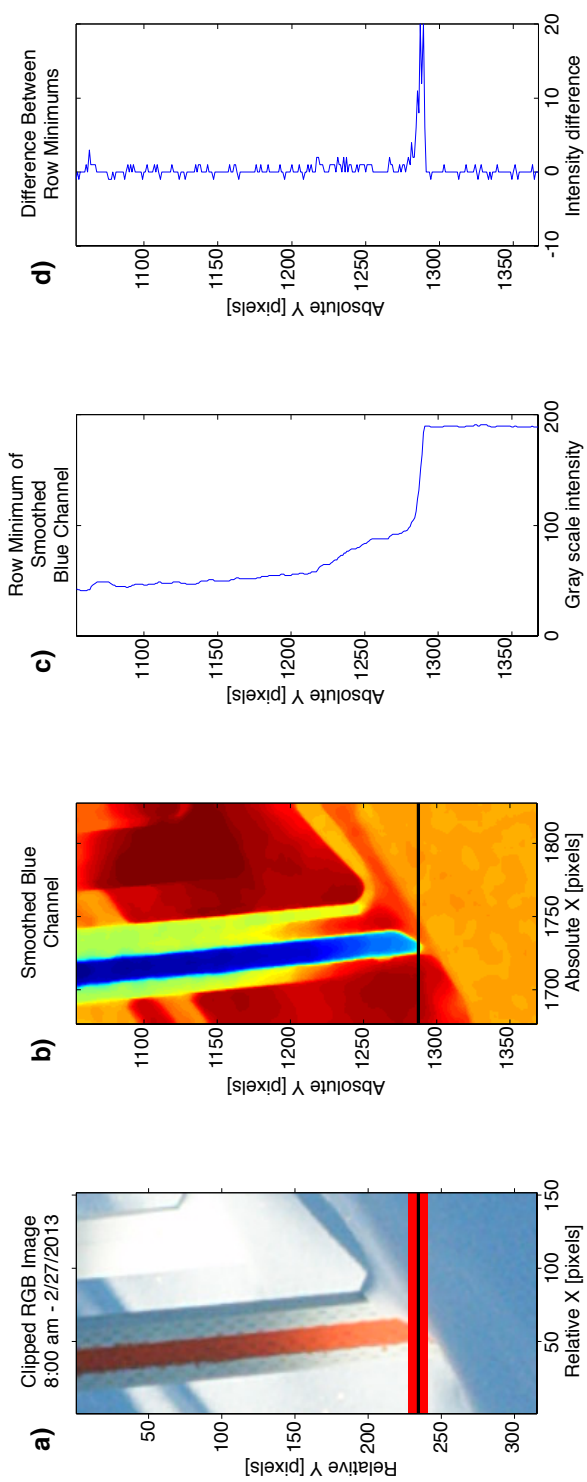


Figure 4.5: Pixel-picking process of SnowDepthCam depth measurement. The thick red line in (a) represents the approximate measurement uncertainty.

4.4 Results

Each day from November 27th, 2012 until the last measurable snow melted on April 25th, 2013, the Bogus Basin time-lapse camera continuously captured hourly images from 8 a.m. to 5 p.m., resulting in 1,500 measurements at two positions spaced 4 meters apart. The high-capacity SD cards that stored the images had plenty of room to spare and the batteries remained dry and in good condition, carrying an 11-Volt load at the conclusion of the season. The ability of the camera to measure hourly snow depths at multiple marker locations proved to be successful. The winter 2012-13 accumulated snow depths for both the near and far marker are shown in Figure 4.6 alongside the depths recorded by the Bogus Basin SNOTEL and Boise State University ultrasonic sensors. The Boise State sensor was not operational until February 26th, within a week of the annual maximum SWE period, and solely captured the melt season evolution. Also, the camera measurements between December 8th–21st were obscured by a large snow-covered tree branch, which was later cleared.

Results of the time-lapse method were also compared to the corresponding LiDAR-derived snow depths obtained from the snow-covered TLS survey on March 13th, 2013. The day was unseasonably warm reaching 13°C at 11am and snow depths obtained by the camera ranged between 81 cm at 8am to 74 cm at 4pm, while the LiDAR-derived snow depth at marker #1 was 70 cm and marker #2 was 74 cm (Figure 4.7).

The motivation for this experiment was to quantify depths of wind drifts at point locations to aid in validation of a wind redistribution model (described in Winstral and Marks (2002) and Chapter 4) in unstable avalanche starting zones. The Canyon Creek camera was installed with the intent to capture the formation of a large drift throughout the winter. Unfortunately, there was no prior information for the sheer

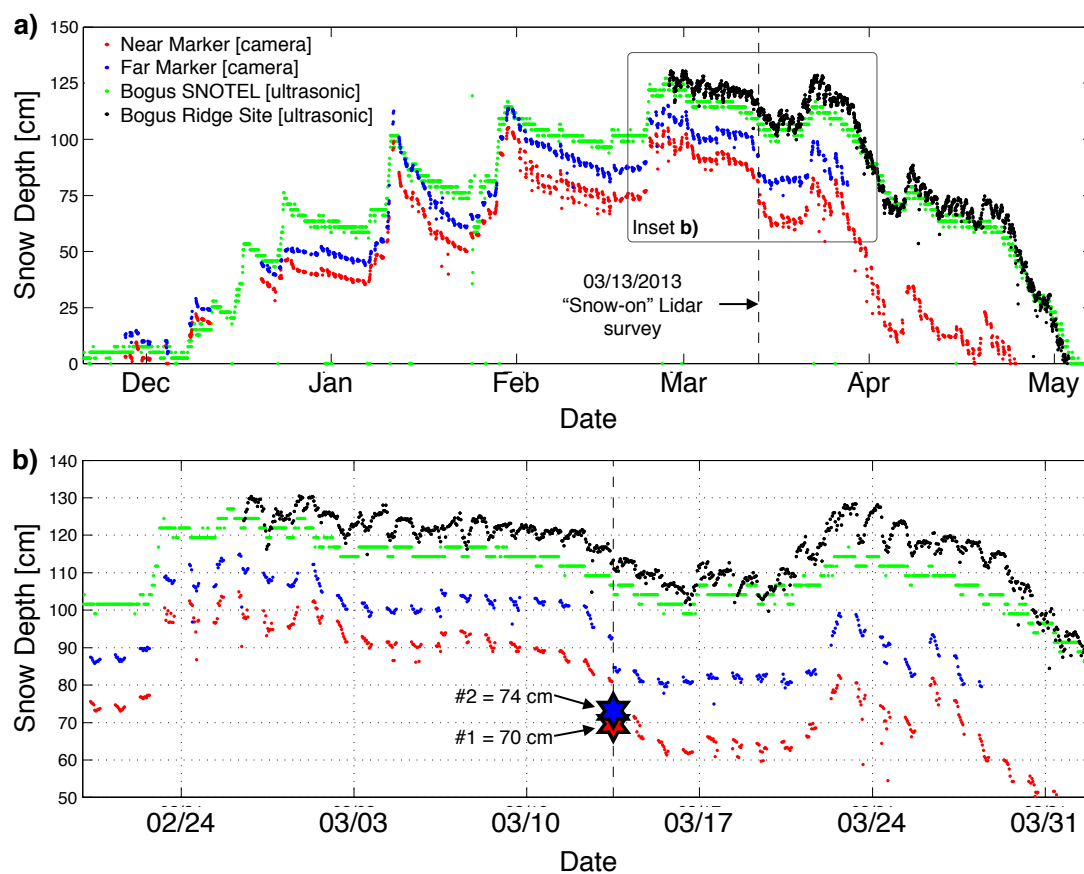


Figure 4.6: **a)**: Winter 2012-13 snow depth accumulation measured by three devices. Red and blue circles represent the near and far depth markers observed by the camera, green circles represent the SNOTEL ultrasonic sensor, and the black circles are the Boise State Hydrology Group ultrasonic sensor. **b)**: Close-up plot showing terrestrial LiDAR snow depth measurements at each marker as red and blue stars.

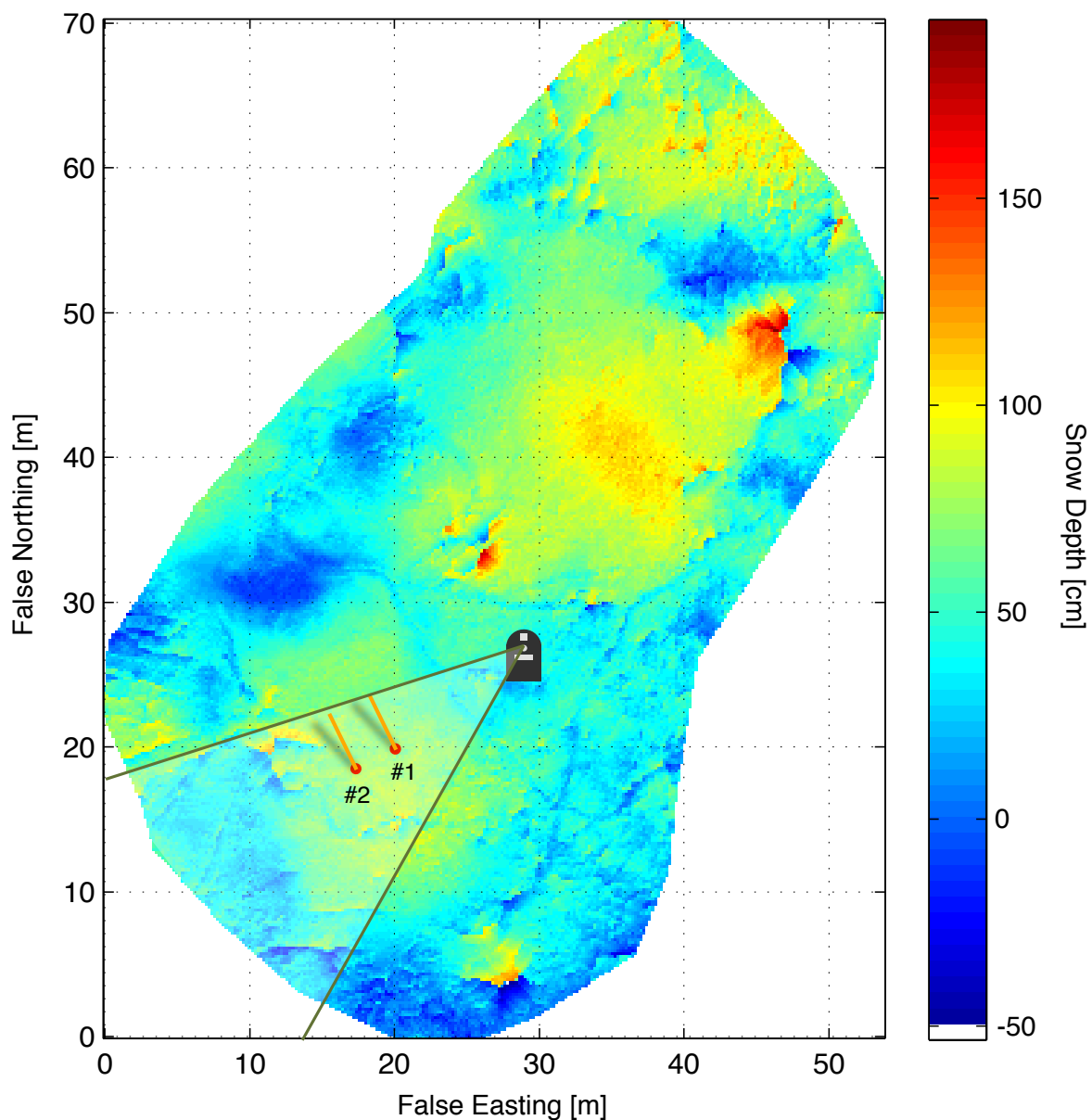


Figure 4.7: Plot of snow depth distribution at the Bogus Basin snow study site obtained by differencing two 20 cm Terrestrial LiDAR-derived DEMs. Time-lapse camera location is shown along with the field-of-view and snow depth markers #1 & #2. Negative snow depth values are due to multiple scan co-registration errors and interpolation edge effects from the LiDAR point cloud.

extent of the drift that would end up obscuring the depth marker by early January. Moreover, exceptionally strong winds that frequented the measurement site caused ice to encapsulate the power connections. As the ice melted, the batteries were shorted and their charge was lost causing the camera to stop working in late January.

4.5 Future Work

As previously mentioned, recording snow depths with time-lapse cameras requires a light source to capture the distributed markers. Up to this point, measurements were only able to be taken during daylight hours, but for the upcoming 2013-2014 winter season two infrared cameras will be tested at the Bogus Basin study site. These will be installed in addition to four standard time-lapse cameras that will be installed along the perimeter of the site and trained upon an array of eight secured depth markers. Another drawback that will be addressed is the lack of real-time data telemetry. The site has an extensive solar power supply in addition to internet access that will be able to transmit images to a central CPU that will process and transmit the snow depth for each marker to a university server.

This time-lapse method holds enormous potential for both avalanche and snow hydrology applications due to the ratio of the low instrumentation cost to the capability to record high resolution snow depth information over distributed spatial scales. Further work will ideally bring about even more portability to make the measurement technique deployable in both locations without year-round power and in dangerous avalanche terrain to monitor accumulation patterns of persistent starting zones.

Method development was funded in part by a research grant from the American Avalanche Association.

CHAPTER 5:

SUMMARY AND CONCLUSIONS

Over the past two decades, the ability to model characteristics of the seasonal snowpack has been drastically enhanced by higher resolution remote sensing methods, weather forecasts, and automated measurements. The primary goal of this research has been to follow in such a way by using a high spatial resolution LiDAR snow accumulation dataset to analyze the effectiveness of an operational hydrologic model. However, using LiDAR to obtain snow depth measurements is not a straightforward process and therefore the data should be validated by manual measurements performed in conjunction with the airborne acquisitions.

Chapter 2 presented a comparison study between the CLPX-II manually-measured and LiDAR-derived snow height changes between Dec. 3rd, 2006 and Feb. 22nd, 2007. Results showed that in shallow snowpacks LiDAR has difficulty resolving changes in snow depth. This occurs because the desired snow depth measurements happen to be at the same scale as the inherent noise (or uncertainty) of the combined LiDAR-interpolated surfaces. In particular, the in situ site with the lowest mean measured change in snow depth (Arapahoe - Figure 2.5) illustrated the inability of LiDAR to correlate with the manual measurements. This has the effect of placing an uncertainty limit of $\approx 15cm$ on the LiDAR observations, which was used in the Chapter 3 model analysis.

Elsewhere in deeper snowpacks the LiDAR tended to under-predict changes in snow depth in comparison to the manual measurements. The best explanation for

this phenomenon is that there exists a large disparity in support between the two measurement techniques. The LiDAR surfaces were interpolated to 5-meter grid cells and then averaged in a 10-meter radius around each reported manual measurement location, whereas the manual measurements are taken by a depth probe with a millimeter-sized tip. This averaging of the LiDAR product, necessarily performed to account for the positional uncertainty of the in situ transects, also has the effect of smoothing out sub-meter scale variations in depth, which are actually sampled by the manual measurements. Yet, when the LiDAR-derived changes in snow depth are viewed as a nearly continuous surface, the sampling shortcomings of manual depth measurements become starkly apparent (Figures 2.5–2.9). A high correlation was ultimately found between mean snow depth changes observed by LiDAR and at all twelve intensive in situ sites. The underestimation of depth changes from the LiDAR observation tended to increase progressively as in situ sites' total average depth and small-scale terrain roughness increased, again likely due to smoothing from taking the mean of previously averaged points around each manual measurement (Figure 2.4).

The CLPX-II LiDAR change in snow depth dataset is so spatially rich and extensive that we next used it for validation of an operational hydrologic modeling data assimilation system. SNODAS, as the model framework is known, assimilates all available snow data to adjust for model shortcomings on a daily time step and at a 30 arc-second (nominally $\approx 1km^2$) resolution. Accordingly, validation datasets must be made independent of readily available automated systems (e.g., SNOTEL and weather station networks), and at the same time cover sufficiently large spatial or temporal scales to match the resolution of model estimates. The comparison of 980 individual SNODAS pixels presented specific areas of higher disagreement between

the model and the LiDAR data.

The area of highest disagreement was in very low accumulation prairie regions. First of all, these environments are notoriously difficult to estimate with hydrological modeling techniques due to myriad physical processes, but also in this case due to a lack of nearby forcing data. Secondly, LiDAR remote sensing uncertainties are on the same order as the total snow depth in these prairie regions, making it impossible to closely resolve absolute snow depths.

In areas where snowpacks are very deep, SNODAS has been found to have some difficulty predicting snow depth and SWE during the accumulation season. Subkilometer-scale spatial variability due to wind redistribution, incident solar radiation, and vegetation interception play an important role in complex mountain terrain, and in these areas SNODAS tends to have increased error in estimates of snow depths. Accounting for hillslope-scale spatial variability in hydrologic models would require *a priori* knowledge of yearly snow distributions. The wind redistribution component of the *Isnobal* snow model provided an accurate method of locating drift and scour regions over a site on the same scale as SNODAS estimate pixels. Future work will distribute the wind redistribution modeling method over larger alpine areas to further study the effect of small-scale variability on the SNODAS modeling method.

Lastly, for the exposed, wind-blown prairie of the North Park region, standard measurement techniques used at SNOTEL stations are not able to capture the spatial variability of snow depths around the site. A new method that may be more suitable in such terrain is to use time-lapse photography for continuous snow depth measurements. A single camera is able to make multiple spatially distributed and non-destructive observations of a snowpack's temporal evolution in landscapes where

ordinary ultrasonic sensors would have considerable difficulty.

The time-lapse photography method for measuring snow depths presented in Chapter 4 can help bridge a data gap for independent validation of hydrologic models like SNODAS. But they will also help researchers study snowpack evolution in dangerous avalanche terrain and remote areas due to their low cost and portability.

In closing, the remote sensing methods presented here (airborne LiDAR and time-lapse photography), though very different in scope and implementation, can be used in concert to quantify spatiotemporal variability of the seasonal snowpack. Future work will focus on the ability to distribute hourly time-lapse measurements of snow depth at multiple locations over vast areas using stored libraries of wind redistribution parameters obtained with airborne LiDAR and meteorological data.

BIBLIOGRAPHY

- Ahn, Y, and Box, J. E. 2010. Glacier velocities from time-lapse photos : technique development and first results from the Extreme Ice Survey (EIS) in Greenland. *Journal of Glaciology*, **56**(198), 723–734.
- Anderson, B. T. 2011. *Spatial Distribution and Evolution of a Seasonal Snowpack in Complex Terrain: An Evaluation of the SNODAS Modeling Product*. Masters Thesis, Boise State University, Boise, Idaho, United States.
- Barnett, T. P, Adam, J. C, and Lettenmaier, D. P. 2005. Potential impacts of a warming climate on water availability in snow-dominated regions. *Nature*, **438**(17), 303–309.
- Barrett, A. P. 2003. National Operational Hydrologic Remote Sensing Center SNOW Data Assimilation System (SNODAS) Products at NSIDC. *NSIDC Special Report 11: Boulder, CO, USA*.
- Beniston, M, Keller, F, Koffi, B, and Goyette, S. 2003. Estimates of snow accumulation and volume in the Swiss Alps under changing climatic conditions. *Theoretical and Applied Climatology*, **76**(3-4), 125–140.
- Cline, D, Yueh, S, Chapman, B, Stankov, B, Gasiewski, A, Masters, D, Elder, K, Kelly, R, Painter, T. H, Miller, S, Katzberg, S, and Mahrt, L. 2009. NASA Cold Land Processes Experiment (CLPX 2002/03): Airborne Remote Sensing. *Journal of Hydrometeorology*, **10**(1), 338–346.

- Clow, D. W, Nanus, L, Verdin, K. L, and Schmidt, J. 2012. Evaluation of SNODAS snow depth and snow water equivalent estimates for the Colorado Rocky Mountains, USA. *Hydrological Processes*, **26**(17), 2583–2591.
- Deems, J. S, Fassnacht, S. R, and Elder, K. J. 2006. Fractal Distribution of Snow Depth from Lidar Data. *Journal of Hydrometeorology*, **7**(2), 285–297.
- Deems, J. S, Fassnacht, S. R, and Elder, K. J. 2008. Interannual Consistency in Fractal Snow Depth Patterns at Two Colorado Mountain Sites. *Journal of Hydrometeorology*, **9**(5), 977–988.
- Deems, J. S, Painter, T. H, and Finnegan, D. C. 2013. Lidar measurement of snow depth: a review. *Journal of Glaciology*, **59**(215), 467–479.
- Elder, K, Dozier, J, and Michaelsen, J. 1991. Snow accumulation and distribution in an alpine watershed. *Water Resources Research*, **27**(7), 1541–1552.
- Erxleben, J, Elder, K, and Davis, R. 2002. Comparison of spatial interpolation methods for estimating snow distribution in the Colorado Rocky Mountains. *Hydrological Processes*, **16**, 3627– 3649.
- Harrison, W. D, Echelmeyer, K. A, Cosgrove, D. M, and Raymond, C. F. 1992. The determination of glacier speed by time-lapse photography under unfavorable conditions. *Journal of Glaciology*, **38**(129), 257–265.
- Hodgson, M. E, and Bresnahan, P. 2004. Accuracy of Airborne Lidar-Derived Elevation : Empirical Assessment and Error Budget. *Photogrammetric Engineering & Remote Sensing*, **70**(3), 331–339.

- Lehning, M, Ingo, V, Gustafsson, D, Nguyen, T. A, Stahli, M, and Zappa, M. 2006. ALPINE3D : a detailed model of mountain surface processes and its application to snow hydrology. *Hydrological Processes*, **20**, 2111– 2128.
- Li, L, and Pomeroy, J. W. 1997. Estimates of Threshold Wind Speeds for Snow Transport Using Meteorological Data. *Journal of Applied Meteorology*, **36**(3), 205–213.
- Liston, G. E, and Sturm, M. 1998. A snow-transport model for complex terrain. *Journal of Glaciology*, **44**(148), 498–516.
- Luce, C. H, Tarboton, D. G, and Cooley, K. R. 1998. The influence of the spatial distribution of snow on basin-averaged snowmelt. *Hydrological Processes*, **12**(10-11), 1671–1683.
- Pinzer, B. R, and Schneebeli, M. 2009. Snow metamorphism under alternating temperature gradients: Morphology and recrystallization in surface snow. *Geophysical Research Letters*, **36**(L23503).
- Prokop, A. 2008. Assessing the applicability of terrestrial laser scanning for spatial snow depth measurements. *Cold Regions Science and Technology*, **54**(3), 155–163.
- Schirmer, M, and Lehning, M. 2011. Persistence in intra-annual snow depth distribution: 2. Fractal analysis of snow depth development. *Water Resources Research*, **47**(W09517), 1–14.
- Seyfried, M. S, and Wilcox, B. P. 1995. Scale and the nature of spatial variability: Field examples having implications for hydrologic modeling. *Water Resources Research*, **31**(1), 173–184.

- Sturm, M, and Wagner, A. M. 2010. Using repeated patterns in snow distribution modeling: An Arctic example. *Water Resources Research*, **46**(12).
- Trujillo, E, Ramírez, J. A, and Elder, K. J. 2007. Topographic, meteorologic, and canopy controls on the scaling characteristics of the spatial distribution of snow depth fields. *Water Resources Research*, **43**(7).
- Winstral, A, and Marks, D. 2002. Simulating wind fields and snow redistribution using terrain-based parameters to model snow accumulation and melt over a semi-arid mountain catchment. *Hydrological Processes*, **16**, 3585– 3603.
- Winstral, A, Marks, D, and Gurney, R. 2009. An efficient method for distributing wind speeds over heterogeneous terrain. *Hydrological Processes*, **23**, 2526– 2535.
- Winstral, A, Marks, D, and Gurney, R. 2013. Simulating wind-affected snow accumulations at catchment to basin scales. *Advances in Water Resources*, **55**(May), 64–79.
- Wiscombe, W. J, and Warren, S. G. 1980. A Model for the Spectral Albedo of Snow. I: Pure Snow. *Journal of the Atmospheric Sciences*, **37**(12), 2712–2733.
- Yueh, S. H, Dinardo, S. J, Akgiray, A, West, R, Cline, D. W, and Elder, K. 2009. Airborne Ku-Band Polarimetric Radar Remote Sensing of Terrestrial Snow Cover. *IEEE Transactions on Geoscience and Remote Sensing*, **47**(10), 3347–3364.